MAESTRÍA EN PROCESAMIENTO DE SEÑALES E IMÁGENES DIGITALES

ESCUELA DE POSGRADO

PONTIFICIA UNIVERSIDAD CATÓLICA DEL PERÚ

Robust Minimum Variance Beamformer using Phase Aberration Correction Methods

Submitted by

Gustavo Chau Loo Kung

In partial fulfillment of the requirements for the Degree of

Master in Digital Signal and Image Processing

in the Graduate School of the Pontificia Universidad Católica del Perú.

Thesis supervised by:

Roberto Lavarello

Jeremy J. Dahl

Examining commitee members:

Roberto Lavarello

Jeremy J. Dahl

Jesse T. Yen

Lima, Perú

February 11, 2017

To God, for blessing me everyday of my life.

To my parents, my siblings and all my family, for their unconditional love.

Jesus looked at them and said, "With man this is impossible, but with God all things are possible".
(Matthew 19,26)

Acknowledgments

"Many times a day I realize how much my own life is built upon the labors of my fellowmen, and how earnestly I must exert myself in order to give in return as much as I have received" - Living Philosophies, Albert Einstein

Everything I am and what I have achieved, including the present work, I own it to all the perople that have helped me throughout my life.

First, I have to thank God for giving me the gift of living and for all the blessings He cast upon me day by day, and for holding me standing in my toughest moments. I deeply thank my parents, for educating me, for correcting me and, overall, for loving and helping me unconditionally. I know I will never be able to repay them all they have given to me. Thanks, mom, for my life and for always being an example of sacrifice and dedication, 媽媽. 多謝駛. 我愛你. Thank you so much dad for your support and example. I will miss you so much, but I know that you are now in the glory of the Lord, that you look out for us from Heaven, and that you will always be by our side. 爸爸，多謝駛,我永遠愛你，愿你在主的庇護下安息. Thanks to all my family: my 阿媽 and my 阿婆, Marina, my sisters Gaby and Carola for all their constant helps and cheerfulness, to my 哥哥 and his wife Tania, and their children, for all their support during my masters, to my 姐姐, Yiyi, and all my cousins. Thanks to my godparents Angélica y Víctor, Rosendo e Iris, my uncles and aunts, especially Lidia, 姑媽, and Blanca.

I also have to thank all the professors that guided me during my graduate studies, especially my advisers Roberto Lavarello and Jeremy Dahl for enabling me to complete this thesis and to present it in front of the scientific community worldwide. Thanks to my funding sources: PUCP grant DGI-2015-3-0016, PUCP Marco Polo grant and Stanford University. Thanks to the members of the comittee: my advisers and Professor Jesse Yen. Thanks to all my friends from the LIM and DSP labs at PUCP and at the Dahl Ultrasonic Lab at Stanford. Thanks to everyone who directly or undirectly has giving me his/her help, advice, time, and guidance throughout these years.

Abstract

The minimum variance (MV) beamformer is an adaptive beamforming method that has the potential to enhance the resolution and contrast of ultrasound images. Although the sensitivity of the MV beamformer to steering vector errors and array calibration errors is well-documented in other fields, in ultrasound it has been tested only under gross sound speed errors. Several robust MV beamformers have been proposed, but have mainly reported robustness only in the presence of sound speed mismatches. Additionally the impact of PAC methods in mitigating the effects of phase aberration in MV beamformed images has not been observed

Accordingly, this thesis report consists on two parts. On the first part, a more complete analysis of the effects of different types of aberrators on conventional MV beamforming and on a robust MV beamformer from the literature (Eigenspace-based Minimum Variance (ESMV) beamformer) is carried out, and the effects of three PAC algorithms and their impact on the performance of the MV beamformer are analyzed (MV-PC). The comparison is carried out on Field II simulations and phantom experiments with electronic aberration and tissue aberrators. We conclude that the sensitivity to speed of sound errors and aberration limit the use of the MV beamformer in clinical applications, and that the effect of aberration is stronger than previously reported in the literature. Additionally it is shown that under moderate and strong aberrating conditions, MV-PC is a preferable option to ESMV.

On the second part, we propose a new, locally-adaptive, phase aberration correction method (LAPAC) able to improve both DAS and MV beamformers that integrates aberration correction for each point in the image domain into the formulation of the MV beamformer. The new method is tested using full-wave simulations of models of human abdominal wall, experiments with tissue aberrators, and *in vivo* carotid images. The LAPAC method is compared with conventional phase aberration correction with delay-and-sum beamforming (DAS-PC) and MV-PC. The proposed method showed between 1-4 dB higher contrast than DAS-PC and MV-PC in all cases, and LAPAC-MV showed better performance than LAPAC-DAS. We conclude that LAPAC may be a viable option to enhance ultrasound image quality of both DAS and MV in the presence of clinically-relevant aberrating conditions.

Keywords

Adaptive beamforming, minimum variance beamformer, phase aberration correction, coherence

Contents

Chapter 1

Introduction

Commercial ultrasound scanners implement the classical delay-and-sum (DAS) beamforming method to form B-mode images. DAS beamforming is subject to the diffraction limit and so its performance is tightly constrained by the physical characteristics of the system. Alternatively, adaptive beamforming techniques have demonstrated that is possible to overcome the diffraction limit. In particular, the Minimum Variance (MV) beamformer exhibits enhanced lateral resolution and contrast in ultrasound images [1]. From other fields, it is known that the MV beamformer is sensitive to calibration and steering vector errors. However, the studies of the sensitivity of the MV beamformer in ultrasound literature has been mainly limited to gross sound speed errors [1, 2].

Although there are several proposed robust minimum variance methods to cope with the problem of sensitivity of the MV beamformer to gross sound speed errors, these approaches normally entail trading-off robustness with a loss in resolution [2, 3, 4]. In the context of this thesis, robustness will be considered as the ability to maintain performance in the presence of aberration. For example, Synevag *et al.* [2] mention that by lowering the subarray smoothing parameter and augmenting the diagonal loading term some robustness against gross sound speed errors can be obtained. This, in turn, causes the MV beamformer to have a performance closer to that of DAS. Wang *et al.* [3] proposed a method to allow the steering vector of the MV beamformer to vary inside an uncertainty ellipsoid. However, this is equivalent to adding an automatically determined amount of diagonal loading, thus making the MV closer to DAS and reducing the resolution [5]. Mehdizadeh *et al.* [4], used forward-backward estimation and a lower rank eigenspace-based approximation are used to increase robustness, but decrease resolution. Xia *et al.* [6] proposed additional constraints to the original MV problem, but the performance was not satisfactory in the presence of near field aberrators.

One key point in these approaches is that the parameters of the smoothing or the steering vector are modified without taking into account potential information that can be estimated using existing phase aberration methods. To the best of our knowledge, the only study of phase aberration correction (PAC) methods in connection with the MV beamformer was presented by Ziksari *et al.* [7] using the nearest neighbor correction method, but the effects of physical and distributed aberration in connection with the MV beamformer were not described.

Giving the state-of-the-art, out contribution is two-fold. First, we do a more complete study of the impact of second order phase aberration errors on the MV beamformer and how PAC correction methods applied prior to the MV beamformer (precorrected MV, MV-PC) can mitigate these effects. We test the

effects of different types of aberration and basic PAC methods on the the original MV beamformer by Synnevag *et al.* [2] we compare this combination with another robust minimum variance beamformer from the literature, the Eigenspace-based minimum variance (ESMV) beamformer [4]. We present results on simulations and experiments with electronic aberration and tissue-based aberrators, which has not previously been reported for MV beamforming. We show that current MV beamforming and robust MV beamforming techniques show great sensitivity to phase aberration and that MV+PAC is a preferable option, even for tissue-based aberrators. This part of the thesis is presented in Chapter 2.

Second, building on the ideas of the first part, we propose a a novel locally adaptive phase aberration correction (LAPAC) technique based on a synthetic aperture multistastic sequence that can correct the arrival time distortions of distributed aberrator in both DAS and MV beamformers. Although the algorithm is applied and compared with both DAS and MV, it enhances more the performance and robustness of the latter.

The method performs an iterative estimation of the profiles at each point in the image domain and performs a correction prior to applying either the DAS or the MV beamformer. A mechanism is included for correction of points where low correlation of the received echoes do not allow a correct estimation of the aberrating phases. We test the new algorithm in full-wave simulations of human abdominal layers, *ex vivo* experiments with beef loin, and an *in vivo* experiment. This part of the thesis is presented in Chapter 3. Finally, the general conclusions of the whole study are presented in 4.

Chapter 2

Part I: Effects of phase aberration and PAC on the MV beamformer

2.1 Methods

2.1.1 Minimum variance beamformers

The MV beamformer is an adaptive beamforming method that, for each point in the image domain, computes the apodization that minimizes the variance of the beamformed signal while maintaining a unitary gain in the presumed direction of arrival. This is done by computing the optimal weights $\mathbf{w}$ that satisfy [2]

$$\mathbf{w} = \frac{\mathbf{R}^{-1}\mathbf{a}}{\mathbf{a}^H\mathbf{R}^{-1}\mathbf{a}}, \tag{1}$$

where $\mathbf{R}$ is the spatial covariance matrix of the signals received at the different array elements and $\mathbf{a}$ is the steering vector. If signals are first pre-steered, as is necessary for the broadband signals in ultrasound imaging, $\mathbf{a}$ reduces to a vector of ones. To estimate $\mathbf{R}$, spatial and time averaging are often employed [2]. Let N represent the number of channels and $\mathbf{x_n}(\mathbf{k})$ be the values of the n-th channel corresponding to time instant k after accounting for the time-of-flight delays. Spatial averaging consists on dividing $\mathbf{x}(\mathbf{k})$ into overlapping subvectors $\mathbf{x}_i(k), i = 1,\ldots,N-L+1$, of length L and obtain an estimate of the covariance matrix, $\hat{\mathbf{R}}(k)$, as

$$\hat{\mathbf{R}}(\mathbf{k}) = \frac{1}{N-L+1}\sum_{i=1}^{N-L+1}\mathbf{x}_i(k)\mathbf{x}_i^H(k). \tag{2}$$

Finally, time averaging is applied by taking the mean of $\hat{\mathbf{R}}(\mathbf{k})$ over a number of time snapshots. In [2], it is stated that by decreasing L and adding a diagonal loading (DL) term, they can accomplish robustness. However, this implementation will be referred as conventional MV beamformer in the present study.

In [4], a new robust MV beamformer, i.e. the eigenspace-based minimum variance beamformer (ESMV), was proposed. The ESMV incorporates two main changes with respect to the standard MV

beamformer. First, a forward-backward averaging is added to the covariance matrix estimation. Second, an eigenspace decomponsition is performed on the forward-backward averaged matrix and only a certain number of eigenvalues are used to reconstruct it.

2.1.2 Phase aberration correction

Phase aberration is normally modelled as either a near-field phase screen (NFPS) aberrator or as a distributed aberrator [8]. In the first model, aberration is approximated as a series of time-shifts that occur at the face of the transducer. The NFPS can be a helpful abstraction when the aberration is concentrated in a thin layer near the transducer, but is less accurate a model for most tissues. In contrast, the distributed aberrator model considers that the source of aberration is distributed throughout the tissue, causing both arrival time fluctuations and waveform distortions. Although it is more accurate and close to real tissue, its complicated nature makes it very difficult to compensate. Most practical implementations of phase aberration correction assume the NFPS model.

Three phase aberration correction methods representative of the literature, i.e., the multi-lag (ML) cross-correlation method [9, 10], Rigby's beamsum method [11], and the scaled covariance matrix (SCM) method [12], were implemented and tested on the simulation and experimental data. The first two were used because they are two common methods used in the phase aberration correction literature [10, 12, 13]. The SCM was selected because it is based on the covariance matrix and it could possibly integrate better with the MV beamforming calculations.

In the ML method, time-shifts between each channel and several neighbor channels are estimated using cross-correlation. Then, these delays are used as the right hand side of an overdetermined system of equations and the aberration profile is obtained from the least squares solution. Multilag cross-correlation estimation was performed with five neighbor channels and an axial window of 2 mm.

In Rigby's beamsum algorithm, the estimated aberrating delays are obtained by correlating each channel signal with the beamsum signal (i.e., the sum of the signals over all channels of the array). The correlation were calculated using a 2 mm length axial window centered at the correction depth.

The SCM algorithm is a modification of Rigby's beamsum algorithm. In this approach, the covariance matrix is formed, then the phase of each matrix element is extracted and these phases are summed across the channels. For computing the covariance matrix, a 2 mm length axial window centered at the correction depth was utilized.

An estimated aberrating profile was obtained with each of these methods for every scanline and for three depths spaced 1 mm above, below and at the transmission focus depth. The profiles obtained for each scanline were laterally averaged. For simulations and electronic aberration, the profiles from all scanlines were averaged to obtain a single profile. For the tissue-based aberrators, groups of five lateral profiles were averaged. The corresponding time shifts were applied only in reception to the simulated or experimental channel data before performing the beamforming process.

2.1.3 Simulations

Two types of simulations were performed using the Field II library[14] with a sampling frequency of 100 MHz. The first simulation consisted of a point target at an axial distance of 40 mm. The second

Figure 1: Tissue sample of beef loin used for the tissue-based aberrator experiments

simulation consisted of an anechoic cyst of 4 mm diameter centered at an axial position of 40 mm. The simulations were performed at a transmission frequency of 5 MHz, using a linear array of 128 elements and a fixed focal number of 2 at 40 mm depth. In both simulations, pre-beamformed data was obtained.

A zero-mean near-field aberration profile of 4 mm correlation length was scaled to RMS strengths of 20 ns, 40 ns, and 60 ns and applied on both transmission and reception. Dynamic focusing was applied on reception with DAS beamforming using a boxcar window and the MV beamformer using a constant spatial smoothing (L) subarray length of 32 elements and a time average of 41 samples [2]. A diagonal loading (DL) term $\mathrm{DL} = \frac{1}{500L}\mathrm{tr}(\mathbf{R})$ was added to the covariance matrices in order to stabilize the inversion of $\mathbf{R}$. The ESMV beamformer used these same parameters and β values of 1% and 10%, as in [4].

2.1.4 Experiments with electronic aberration

Experimental data was obtained from a multipurpose phantom model 539 (ATS Laboratories, Connecticut, USA) using a Verasonics V1 acquisition system (Verasonics Inc, Washington, USA) with a 128 element transducer at a central frequency of 5 MHZ and a sampling frequency of 20 MHz. Channel data was acquired from both point targets and anechoic cyst targets of 2 mm radius of the phantom. Aberration profiles of 4 mm correlation length and strengths of 0, 20, 40 and 60 ns were applied both in transmission and reception. A single transmission focus was used (30 mm for the point targets and 35 mm for the cyst targets) and the focal number was set at 2. Dynamic focusing was applied on reception. The parameters for the MV beamformer and the ESMV were the same as for the simulations.

2.1.5 Experiments with tissue aberrators

Two sections of beef loin were used as tissue aberrators. They had thicknesses of 2 cm (Aberrator A) and 2.8 cm (Aberrator B), respectively.

Each beef loin section was placed on top of the multipurpose ATS phantom and the transducer was placed on top of beef loin. The experimental setup for aberrator A is shown in Figure 1. The same system configuration and data acquisition procedure used with the electronic aberrators was used to acquire channel data from the cyst target zones of the phantom. Control data at the same approximate position but with no tissue between the transducer and the phantom were obtained to measure the effects of aberration and PAC.

2.1.6 Comparison and metrics

For both simulated and experimental datasets, data is beamformed using DAS, DAS combined with each of the three mentioned PAC methods, MV, MV with each of the three mentioned PAC methods and ESMV with beta values of 1% and 10%.

For the dataset with point reflectors, the performance of the different beamforming methods are assessed in terms of full width at half maximum (FWHM) and peak sidelobe level (PSL). For all datasets containing anechoic inclusions, contrast and contrast-to-noise ratio (CNR) are computed according to the following formulas

$$\text{Contrast} = 20\log\left(\frac{\mu_1}{\mu_0}\right)$$

$$\text{CNR} = \frac{|\mu_1 - \mu_0|}{\sqrt{0.5(\sigma_1^2 + \sigma_0^2)}},$$

where μ_1 and μ_0 are the mean values of the region of interest (ROI) and background, respectively and σ_1^2 and σ_0^2 are the variances of the ROI and the background, respectively.

For simulations and experiments with electronic aberration, as the aberration profile applied to the data is known, the residual error in the estimation of the aberration profiles was quantified by subtracting the applied profile from the profiles estimated at every lateral position and computing the mean absolute error. For the case of tissue aberrators, as the ground truth profile is not known, the aberrators were only characterized in terms of aberration strength (in ns) and correlation length (in mm). Additionally, some computational times are presented for the different PAC methods and beamforming methods. All tests were performed using a standard portable computer with a Intel core i7 processor and 8 Gb of RAM.

For the electronic aberration and tissue aberrator cases, the experimental data was contaminated by a gross speed error, which presented itself as geometric delays of parabolic shape. This error can be attributed to variation in speed of sound of the phantom from the nominal phantom speed value of 1450 m/s. Therefore, the best-fit second order polynomial was subtracted from the estimated time-shifts to obtain the final aberration profile for the error estimation or characterization.

2.2 Results

2.2.1 Simulations Results

B-mode images for the point target simulations are shown in Fig. 2 for the case of 60 ns of aberration. The first row consists of the control image of DAS (no aberration), DAS at 60 ns with no correction,

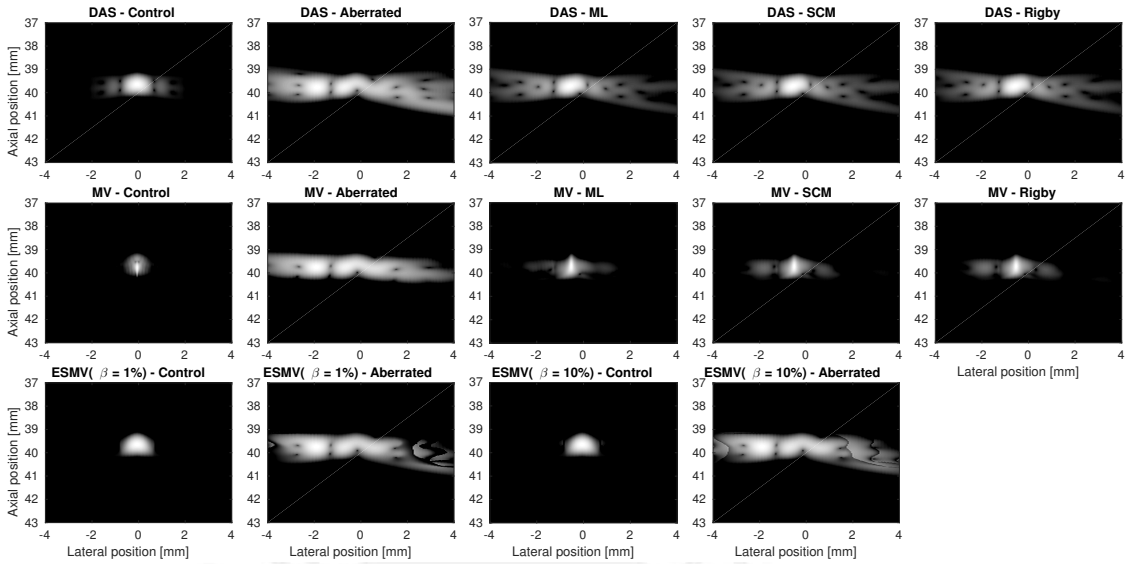

Figure 2: B-mode images of the simulated point targets with 60 ns aberration and control data with no aberration. The top row depicts DAS images for the no aberration, aberrated and corrected cases. The second row shows the same but for conventional MV. The third row show the ESMV control and aberrated images with two β values.

and DAS at 60 ns with the three correction methods. The second row depicts the same images for MV. The third row shows control and aberrated images for ESMV. All images are shown at a dynamic range of 50 dB. At this particular aberration strength, the aberrated MV images are degraded almost as much as the DAS images.

The FWHM and PSL values are shown in Tables I and II, respectively. The percent change with respect to the non-aberrated case are also shown in parentheses. From these results, it can be observed that while DAS exhibited lost of a maximum of 28% in FWHM for the strongest aberration, MV had a degradation of more than 400%. The ESMV had a resolution similar to that of DAS in the no aberration case and showed more robustness than regular MV, as it presented degradations of around 30%. For the case of PSL, DAS exhibited degradations of up to 99% while MV exhibited degradations of up to 96%. ESMV was slightly more robust, with PSL increasing by around 90%. For the case of the simulations, it is observed in Tables I and II that, in DAS, ML reduced degradation of FWHM from 28% to 22% and of PSL from 99% to 43%. Meanwhile, this same method converted a degradation for the MV beamformer of nearly 450% to a degradation of only 6% in FWHM, and of 96% to 24% in PSL.

The simulated cyst target images are shown in Fig. 3. The first row shows the control image for DAS (no aberration), DAS at 60 ns with no correction, and DAS at 60 ns with the three correction methods. The second row depicts the same but for MV. The third row shows control and aberrated images for ESMV. All images are shown with a dynamic range of 50 dB. The ROI for the contrast and CNR calculations was taken as circle of radius 1.8 mm centered at 0 mm lateral position and 40 mm axial position that is inside the anechoic cyst. The background values corresponded to a circle of the same radius but centered at a lateral position of -3 mm and at the same depth. Results for contrast and CNR are displayed in Tables XXII and XXIII. It is observed that DAS contrast was reduced by up to 87% while MV contrast was reduced by up to 89%. Similar maximum degradations were observed for the ESMV. Although MV and ESMV exhibited 5 or more dB higher contrast than DAS at 0 ns

Table I: Full-width at half-maximum (in mm) for the simulated point targets at different aberration strengths and beamforming methods. The percent change from the no aberration case is shown in parentheses.

	Full-width at half-maximum (mm)			
Aberration strength	**0 ns**	**20 ns**	**40 ns**	**60 ns**
DAS	0.61	0.63 (3%)	0.72 (18%)	0.78 (28%)
DAS + ML	0.61	0.63 (3%)	0.65 (8%)	0.74 (22%)
DAS + SCM	0.61	0.62 (1%)	0.65 (8%)	0.73 (20%)
DAS + Rigby	0.61	0.63 (3%)	0.65 (7%)	0.7 (15%)
MV	0.15	0.53 (255%)	0.72 (387%)	0.8 (441%)
MV + ML	0.15	0.16 (5%)	0.15 (2%)	0.16 (6%)
MV + SCM	0.15	0.18 (21%)	0.17 (17%)	0.19 (31%)
MV + Rigby	0.15	0.17 (18%)	0.21 (43%)	0.21 (42%)
ESMV ($\beta = 1\%$)	0.59	0.67 (14%)	0.72 (23%)	0.8 (37%)
ESMV ($\beta = 10\%$)	0.59	0.68 (16%)	0.74 (27%)	0.78 (33%)

Table II: Peak sidelobe level (in dB) for the simulated point targets at different aberration strengths and beamforming methods. The percent change from the no aberration case is shown in parentheses.

	Peak sidelobe level (dB)			
Aberration strength	**0 ns**	**20 ns**	**40 ns**	**60 ns**
DAS	-30.6	-23 (24.8%)	-8.5 (72.2%)	-0.3 (99%)
DAS + ML	-30.6	-25.9 (15.3%)	-21.6 (29.5%)	-17.3 (43.6%)
DAS + SCM	-30.6	-26.8 (12.5%)	-21.4 (30.3%)	-17.5 (42.9%)
DAS + Rigby	-30.6	-26.4 (13.6%)	-21.4 (30.2%)	-16.9 (44.8%)
MV	-44.8	-20.8 (53.7%)	-8.3 (81.6%)	-2.1 (95.3%)
MV + ML	-44.8	-40 (10.8%)	-39.7 (11.5%)	-34.2 (23.6%)
MV + SCM	-44.8	-43.4 (3.2%)	-37.5 (16.4%)	-29.6 (33.9%)
MV + Rigby	-44.8	-42.3 (5.6%)	-32.5 (27.4%)	-27.9 (37.8%)
ESMV ($\beta = 1\%$)	-59.2	-28.9 (51.1%)	-9.3 (84.3%)	-4.4 (92.5%)
ESMV ($\beta = 10\%$)	-42.8	-28.5 (33.4%)	-9.7 (77.3%)	-4.5 (89.4%)

of aberration, at 60 ns the performance of MV, ESMV and DAS were almost equivalent. This is also reflected in the B-mode images where the cyst is difficult to identify. A similar effect was observed for the CNR, where DAS degraded by 68%, MV degrades by 64% and ESMV degrades by 70%. The application of ML reduced the degradation for DAS in constrast (from 87% to 52%) and CNR (from 67% to 24%). Meanwhile, for MV the reductions in degradations were more noticeable, i.e. from 89% to 41% in contrast and from 69% to 3% in CNR.

The mean and standard deviation of the profile estimation errors are reported in Table VI for the point targets and in Table VII for the cyst targets. It is observed that as aberration strength increased the error in the estimation increased and that error is on average higher for the case of speckle based targets.

The speckle resolution obtained with the different techniques is showed in Table V. It can be observed that resolution is not too different among DAS, MV and ESMV.

Additionally, some computational results for the estimation of a 128 element profile are presented in tables VIII. The average time needed to compute the whole profile is specified in seconds. The average time (in milliseconds) needed to compute one point in the image domain for each of the different beamforming methods is shown in IX.

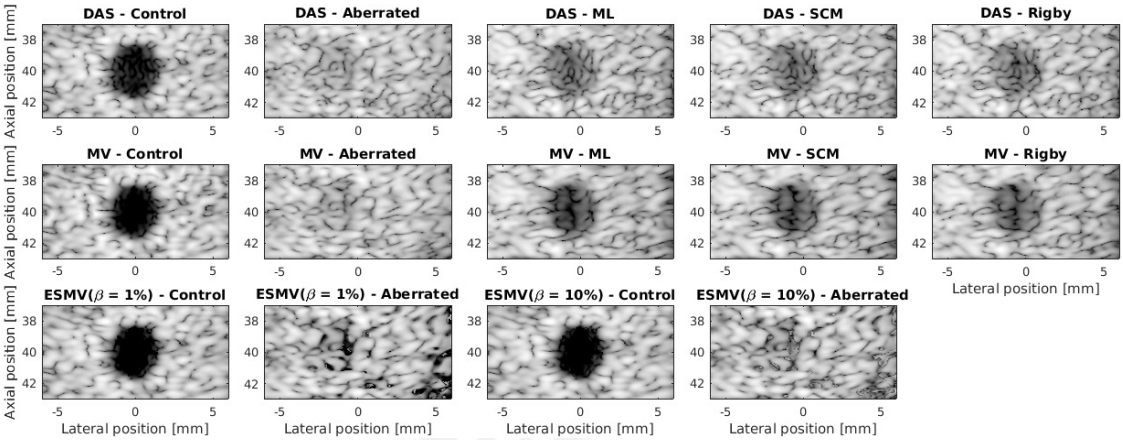

Figure 3: B-mode images of the simulated cyst targets with 60 ns aberration and control data with no aberration. The top row depicts DAS images for the no aberration, aberrated and corrected cases. The second row shows the same but for conventional MV. The third row show the ESMV control and aberrated images with two β values.

Table III: Contrast (in dB) for the simulated anechoic cyst at different aberration strengths and beamforming methods. The percent change from the no aberration case is shown in parentheses.

	Contrast (dB)			
Aberration strength	**0 ns**	**20 ns**	**40 ns**	**60 ns**
DAS	36.1	19 (-47%)	7.4 (-79%)	4.6 (-87%)
DAS + ML	36.1	26.7 (-26%)	21.5 (-40%)	17.2 (-52%)
DAS + SCM	36.1	26.7 (-26%)	20.6 (-43%)	16.6 (-54%)
DAS + Rigby	36.1	26.5 (-26%)	19.4 (-46%)	16.2 (-55%)
MV	41.8	21.5 (-49%)	8.6 (-79%)	4.5 (-89%)
MV + ML	41.8	32.7 (-22%)	25.1 (-40%)	24.5 (-41%)
MV + SCM	41.8	33.8 (-19%)	26 (-38%)	21.5 (-49%)
MV + Rigby	41.8	34.1 (-18%)	22.6 (-46%)	19.1 (-54%)
ESMV (1%)	47	29 (-38%)	12.7 (-73%)	5.4 (-88%)
ESMV (10%)	44.7	26.7 (-40%)	11.2 (-75%)	4.9 (-89%)

Table IV: Contrast-to-noise ratio for the simulated anechoic cyst at different aberration strengths and beamforming methods. The percent change from the no aberration case is shown in parentheses.

	Contrast-to-noise Ratio			
Aberration strength	**0 ns**	**20 ns**	**40 ns**	**60 ns**
DAS	2.17	2.10 (-3.1%)	1.02 (-52.9%)	0.71 (-67.5%)
DAS + ML	2.17	2.29 (5.5%)	2.18 (.5%)	1.65 (-24.1%)
DAS + SCM	2.17	2.29 (5.4%)	2.16 (-.5%)	1.65 (-24.2%)
DAS + Rigby	2.17	2.29 (5.3%)	2.13 (-2.1%)	1.65 (-24.2%)
MV	1.85	2.14 (15.8%)	1.16 (-36.9%)	0.66 (-64.2%)
MV + ML	1.85	2.28 (23.5%)	2.28 (23.5%)	1.78 (-3.3%)
MV + SCM	1.85	2.28 (23.5%)	2.27 (23.1%)	1.72 (-6.5%)
MV + Rigby	1.85	2.28 (23.5%)	2.21 (19.8%)	1.67 (-9.3%)
ESMV (1%)	2.13	2.31 (8.5%)	1.34 (-36.8%)	0.62 (-70.9%)
ESMV (10%)	2.12	2.28 (7.5%)	1.29 (-39.4%)	0.59 (-72.4%)

Table V: Speckle size for the simulations at different aberration strengths and beamforming methods.

	Speckle size (mm)			
Aberration strength	**0 ns**	**20 ns**	**40 ns**	**60 ns**
DAS	2.04	1.89	2.04	2.33
DAS + ML	2.04	1.89	2.04	2.33
DAS + SCM	2.04	1.89	1.89	2.33
DAS + Rigby	2.04	1.89	1.89	2.33
MV	1.89	1.89	2.18	2.47
MV + ML	1.89	1.89	2.04	2.33
MV + SCM	1.89	1.89	1.89	2.33
MV + Rigby	1.89	1.89	2.04	2.33
ESMV (1%)	2.04	1.89	2.04	2.33
ESMV (10%)	2.04	1.89	2.04	2.33

Table VI: Mean residual error of estimated profile for simulated point targets

	Mean error $\pm$ standard deviation (ns)		
Aberration	**ML**	**SCM**	**Rigby**
20 ns	11.7 ± 0.3	12.9 ± 3.3	12.6 ± 1.6
40 ns	23.3 ± 0.2	23.7 ± 1.4	23.7 ± 1.4
60 ns	34.9 ± 0.2	35.5 ± 1.8	35.4 ± 1.1

2.2.2 Experiments with electronic aberration

B-mode images for the point targets with an electronic aberration of 40 ns are displayed in Fig. 4 and, for the cyst targets, with the same aberration in Fig. 5.

The errors in the estimation of aberration profiles for both point target and cyst targets experiments are shown in Tables X and XI, respectively.

The FWHM and PSL for the point target at 30 mm depth are shown in Tables XII and XIII. The degradation from the 0 ns case is shown in parentheses. FWHM decreases by 5% for DAS and 147% for MV. ESMV shows a higher degree of robustness in this case, degrading by only 70%. PSL degrades by 70-90% in all cases.

With ML, the degradation in FWHM is reduced from 5% to 2% in DAS and from 147 % to 20% for MV. Reductions in degradation of PSL from around 80% to around 30% for both DAS and MV are also obtained.

The cyst located approximately at a lateral position of 0 mm and at an axial position of 40 mm was analyzed in terms of contrast and CNR. The ROI was taken as a circle of radius 1.8 mm within the cyst and in the background. The contrast (Table XIV) and CNR (Table XV) were calculated for these regions. As seen on these tables, the degradation in contrast was around 83% for DAS and 90% for both conventional MV and ESMV at the highest aberration strength. Similar trends were observed in

Table VII: Mean error of estimated profile for simulated cyst targets

	Mean error$\pm$ standard deviation (ns)		
Aberration	**ML**	**SCM**	**Rigby**
20 ns	13.1 ± 1.4	15.9 ± 4	14.9 ± 3.2
40 ns	24.2 ± 1.2	28.2 ± 4.5	27.6 ± 4
60 ns	36.7 ± 2.5	40.2 ± 5.4	40.5 ± 7

Table VIII: Average time in seconds for the estimation of the aberration profile

	ML	SCM	Rigby
Average Time (seconds)	10.2	1.56	1.52

Table IX: Average time in milliseconds for computing one point in the image domain using the different beamforming methods

	DAS	MV	ESMV
Average Time (ms)	0.0001	1.1288	1.468

CNR: DAS losses 70% of CNR at 60 ns while MV and ESMV loss between 83% and 90%. On the other hand, contrast and CNR were greatly improved by ML in the case of MV. The degradations were diminished from 92% to 24% for contrast and from 64% to 3% for CNR. Although ML conveyed the highest improvements, the improvements of the other two PAC methods were quite similar.

2.2.3 Experiments with tissue aberrators

B-mode images for tissue aberrator A and tissue aberrator B are displayed in Figures 6 and 7, respectively. The characterization of both tissue aberrators with the different PAC methods is shown in Table XVI for aberrator A and in Table XVII for aberrator B as the mean value $\pm$ standard deviation. It is observed that aberrator B was estimated to have almost double the strength of aberrator A.

For the quantitative comparison, the cysts located aproximately at an axial position of 40 mm and

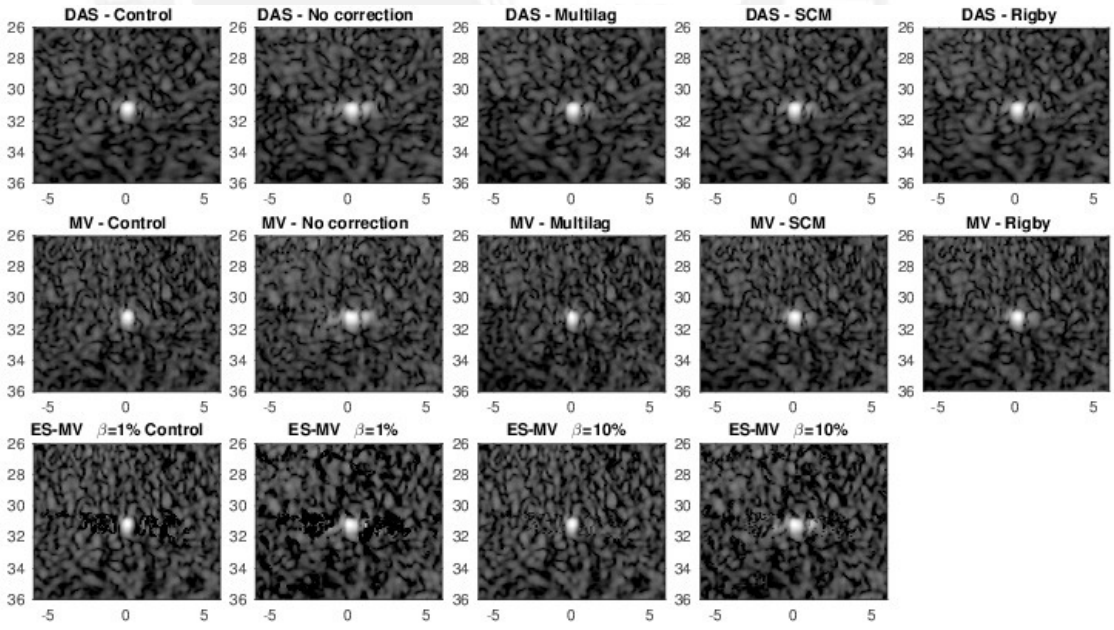

Figure 4: B-mode images of the experimental point targets corrupted with electronic aberration of 40ns strength. The top row depicts DAS images for the no aberration, aberrated and corrected cases. The second row shows the same but for conventional MV. The third row shows the ESMV control and aberrated images.

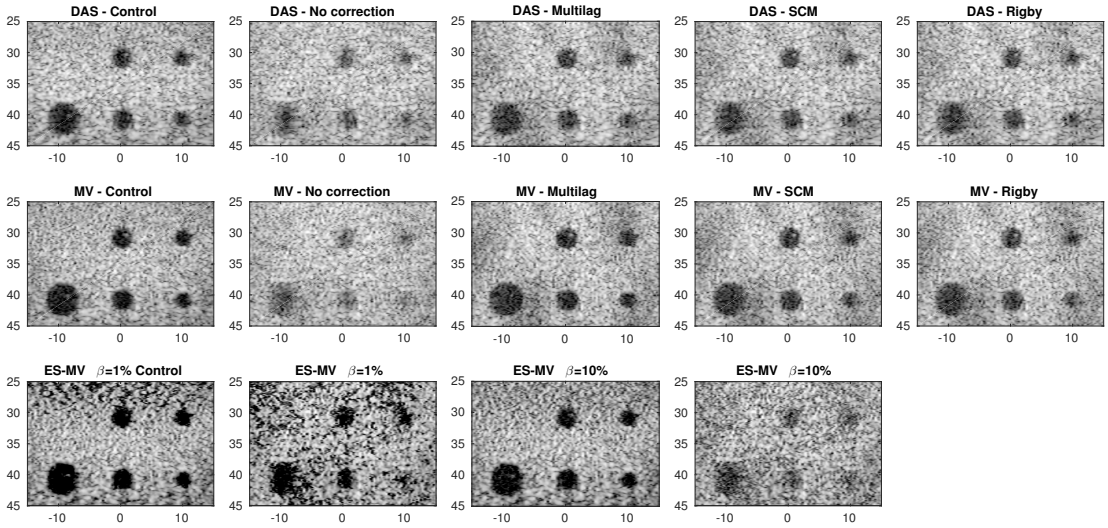

Figure 5: B-mode images of the experimental cyst targets corrupted with electronic aberration of 40 ns strength. The top row depicts DAS images for the no aberration, aberrated and corrected cases. The second row shows the same but for conventional MV. The third row shows the ESMV control and aberrated images.

Table X: Mean error of estimated profile for the point targets with electronic aberration

	Mean error ± standard deviation (ns)		
Aberration	**ML**	**SCM**	**Rigby**
20 ns	12.8 ± 3.9	25.4 ± 13.6	25.1 ± 13.9
40 ns	19.2 ± 5.1	29.2 ± 11.9	28.6 ± 0.11
60 ns	28.7 ± 7.5	34.5 ± 10.2	34.6 ± 10.8

lateral positions of 0 mm and 10 mm were analyzed. The ROIs were taken as a circle of radius 1.8 mm within the cyst and in the background. For the cyst at 0 mm lateral position, the contrast is shown in Table XVIII and the CNR is shown in Table XIX. As seen on these tables, contrast was reduced by 19% and 49% for DAS, by 37% and 65% for MV and by around 20% and 60% for ESMV for aberrator A and B, respectively. For the cyst at a lateral position of 10 mm, the constrast is shown in Table XX and the CNR is shown in Table XXI. In this case, contrast was reduced by 19% and 18% for DAS, by 31% and 42% for MV and by 43% and 48% for ESMV, for aberrators A and B, respectively.

On the other hand, the application of PAC methods reduce the degradation effects of the physical aberrators, more noticeably in the highly aberrating layer (aberrator B). For instance, degradations of 65% in contrast and 43% in CNR were reduced to 38% and 10%, respectively. These enhancements allowed MV+PAC to have better contrast and CNR than DAS+PAC and ESMV for the cyst at 0 mm

Table XI: Mean error of estimated profile for the cyst targets with electronic aberration

	Mean error ± standard deviation (ns)		
Aberration	**ML**	**SCM**	**Rigby**
20 ns	11.6 ± 2.1	17.3 ± 5	16.76 ± 4.3
40 ns	18.8 ± 2.9	25.9 ± 5.4	25.6 ± 5.6
60 ns	30.51 ± 6.5	34.6 ± 7.3	34.7 ± 7

Table XII: FWHM for the experimental point target at 30 mm depth with different electronic aberration strengths and beamforming methods. The percent change from the no aberration case is shown in parentheses.

	Full-width at half-maximum (mm)			
Aberration strength	**0 ns**	**20 ns**	**40 ns**	**60 ns**
DAS	0.54	0.55 (0.9%)	0.55 (2.0%)	0.57 (5.5%)
DAS + ML	0.54	0.54 (-0.6%)	0.53 (-1.0%)	0.53 (-2.1%)
DAS + SCM	0.54	0.52 (-3.0%)	0.52 (-3.8%)	0.53 (-2.5%)
DAS + Rigby	0.54	0.53 (-2.5%)	0.52 (-3.2%)	0.52 (-3.4%)
MV	0.29	0.38 (33.6%)	0.59 (105.5%)	0.71 (147.1%)
MV + ML	0.29	0.31 (6.9%)	0.31 (9.3%)	0.52 (80.4%)
MV + SCM	0.29	0.32 (13.0%)	0.29 (1.1%)	0.35 (20.4%)
MV + Rigby	0.29	0.34 (18.3%)	0.33 (15.1%)	0.40 (38.1%)
ESMV (1%)	0.36	0.36 (.2%)	0.57 (57.8%)	0.61 (69.2%)
ESMV (10%)	0.36	0.36 (.2%)	0.57 (57.8%)	0.61 (69.2%)

Table XIII: PSL for experimental point target at 30 mm depth with different electronic aberration strengths and beamforming methods. The percent change from the no aberration case is shown in parentheses.

	Peak sidelobe level (PSL)			
Aberration strength	**0 ns**	**20 ns**	**40 ns**	**60 ns**
DAS	-28.0	-19.9 (29%)	-12.2 (56.4%)	-5.8 (79.3%)
DAS + ML	-28.0	-24.2 (13.8%)	-20.6 (26.7%)	-14.7 (47.6%)
DAS + SCM	-28.0	-24.8 (11.5%)	-21.1 (24.9%)	-18.7 (33.2%)
DAS + Rigby	-28.0	-23 (18%)	-21 (25%)	-17.4 (38.1%)
MV	-31.0	-21.8 (29.7%)	-12.3 (60.4%)	-5.1 (83.6%)
MV + ML	-31.0	-27.3 (11.9%)	-24.3 (21.7%)	-14.2 (54.2%)
MV + SCM	-31.0	-28.7 (7.4%)	-27.5 (11.4%)	-21.4 (31.1%)
MV + Rigby	-31.0	-27.4 (11.5%)	-26.7 (13.9%)	-20.3 (34.5%)
ESMV (1%)	-30.1	-23.9 (20.5%)	-11.7 (61.2%)	-3.1 (89.6%)
ESMV (10%)	-30.1	-23.9 (20.5%)	-11.7 (61.2%)	-3.1 (89.6%)

lateral position.

Table XIV: Contrast (in dB) for the experimental cyst target at 40 mm depth at different electronic aberration strengths and beamforming methods. The percent change from the no aberration case is shown in parentheses.

	Contrast of cyst at 40 mm (dB)			
Aberration strength	**0 ns**	**20 ns**	**40 ns**	**60 ns**
DAS	17.3	15.2 (-12%)	8.9 (-49%)	3.0 (-83%)
DAS + ML	17.3	18 (4%)	17.8 (3%)	15.0 (-13%)
DAS + SCM	17.3	18 (4%)	17.0 (-1%)	14.7 (-15%)
DAS + Rigby	17.3	17.8 (3%)	16.1 (-7%)	13.1 (-24%)
MV	24	17.1 (-29%)	8.3 (-65%)	1.9 (-92%)
MV + ML	24.0	23.5 (-2%)	22.0 (-8%)	18.3 (-24%)
MV + SCM	24.0	23 (-4%)	19.7 (-18%)	16.5 (-31%)
MV + Rigby	24.0	22.7 (-6%)	18.2 (-24%)	14.7 (-39%)
ESMV (1%)	29.4	24.3 (-17%)	15.7 (-47%)	1.6 (-94%)
ESMV (10%)	25.9	20.6 (-20%)	9.8 (-62%)	1.7 (-93%)

Table XV: Contrast-to-noise ratio for the experimental cyst target located at 40 mm depth with different electronic aberration strengths and beamforming methods. The percent change from the no aberration case is shown in parentheses.

	CNR of cyst at 40 mm			
Aberration strength	**0 ns**	**20 ns**	**40 ns**	**60 ns**
DAS	2.17	2.09 (-3.7%)	1.60 (-26.2%)	0.66 (-69.6%)
DAS + ML	2.17	2.29 (5.2%)	2.36 (8.4%)	2.35 (8.3%)
DAS + SCM	2.17	2.28 (4.9%)	2.34 (7.8%)	2.37 (9.2%)
DAS + Rigby	2.17	2.27 (4.3%)	2.28 (4.7%)	2.25 (3.5%)
MV	2.49	2.35 (-5.5%)	1.65 (-33.7%)	0.40 (-83.9%)
MV + ML	2.49	2.51 (.7%)	2.49 (.1%)	2.60 (4.2%)
MV + SCM	2.49	2.52 (1.3%)	2.51 (.8%)	2.65 (6.4%)
MV + Rigby	2.49	2.51 (1%)	2.51 (.7%)	2.60 (4.6%)
ESMV (1%)	2.13	2.24 (4.9%)	1.61 (-24.5%)	0.21 (-90.2%)
ESMV (10%)	2.10	2.16 (3%)	1.45 (-30.9%)	0.26 (-87.7%)

2.3 Discussion

2.3.1 Degradation caused by phase aberration

The simulations and experiments verify that MV is much more sensitive to aberration than DAS than previously indicated [1, 2]. For instance, the resolution of MV starts four times better than DAS's

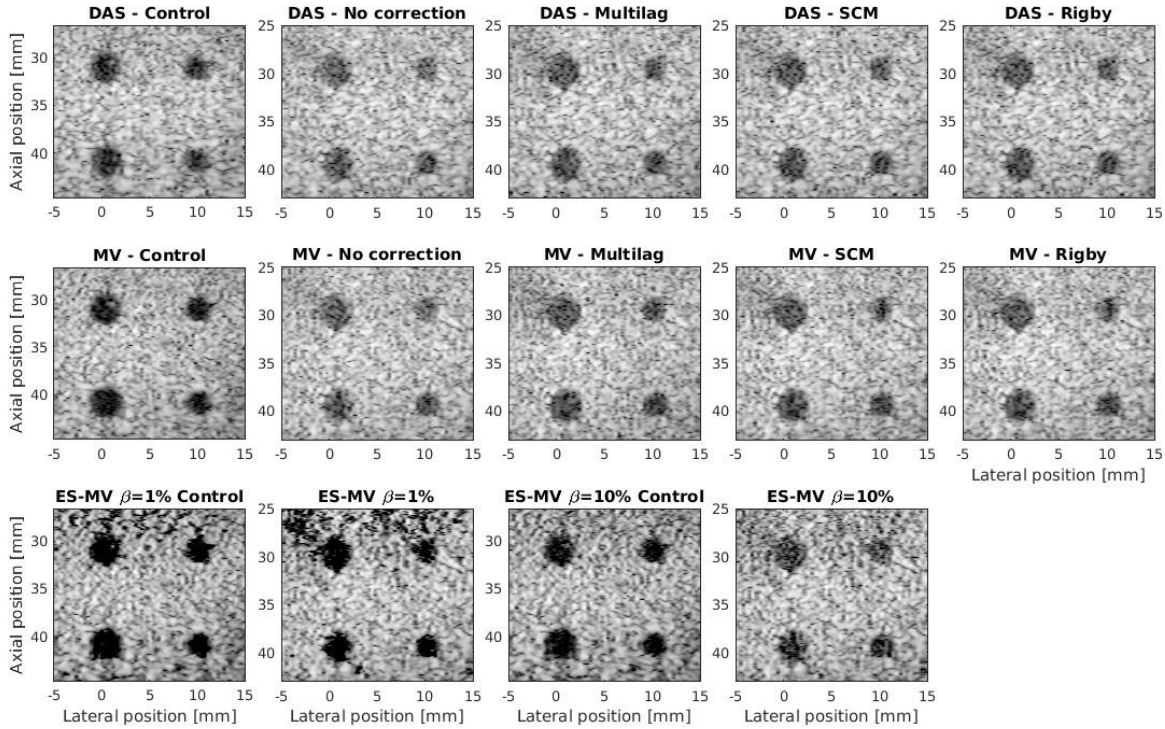

Figure 6: B-mode images of the experimental cyst targets corrupted with aberrator A. The top row depicts DAS images for the no aberration, aberrated and corrected cases. The second row shows the same but for conventional MV. The third row show the ESMV control and aberrated images with two β values.

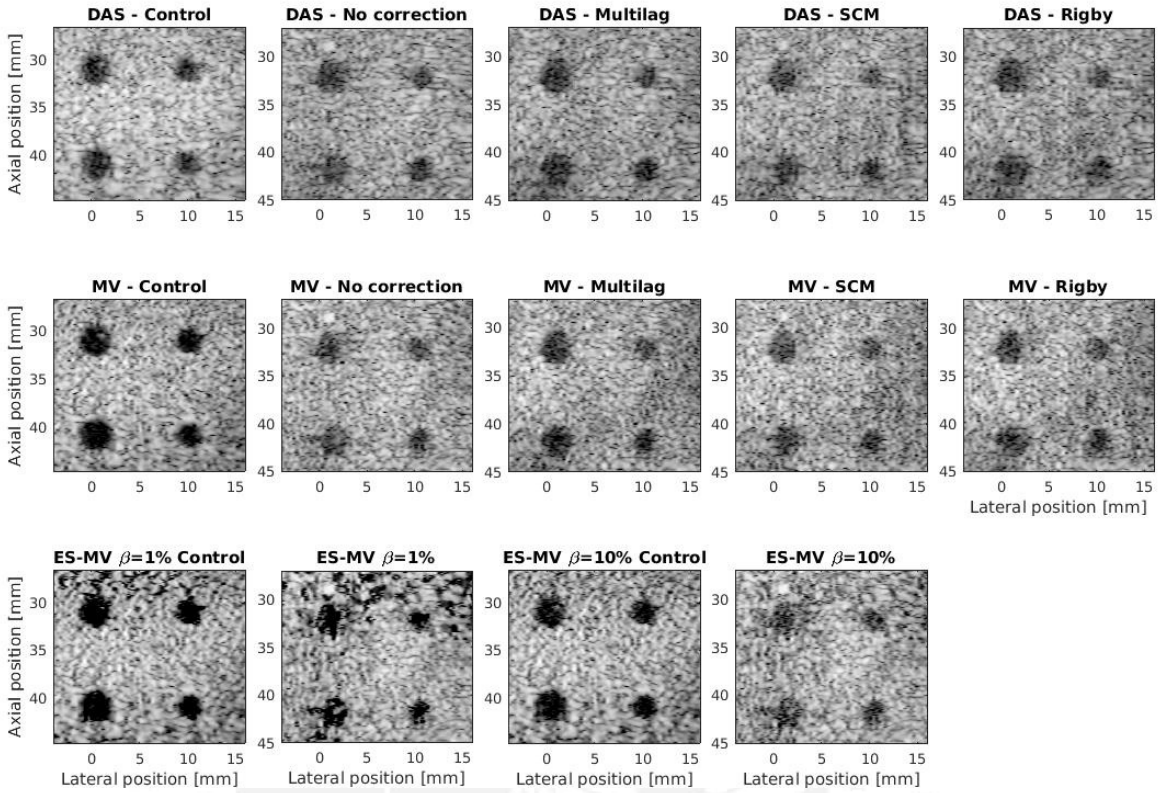

Figure 7: B-mode images of the experimental cyst targets corrupted aberrator B. The top row depicts DAS images for the no aberration, aberrated and corrected cases. The second row shows the same but for conventional MV. The third row show the ESMV control and aberrated images with two β values.

Table XVI: Characterization of estimated profile for the tissue aberrator A.

Method	Aberration strength(ns)	correlation length (mm)
ML	22 ± 2.7	2.47 ± 0.58
SCM	28 ± 8.3	2.53 ± 0.94
Rigby	27 ± 9.4	2.47 ± 1.08

but for the case of the strongest aberration, i.e. 60 ns, the lateral resolution of MV is worse than that of DAS. In the case of PSL, the sidelobes in MV beamforming with no aberration are around 15 dB lower than those of DAS, but even at low aberration values the sidelobes are almost equivalent to DAS. ESMV had an initial FWHM closer than that of DAS and also presented some degree of robustness in this regard but the PSL of ESMV degraded almost as quickly as that of regular MV. This behavior was also reflected in the anechoic inclusion simulations. The contrast of simulated cysts for MV and DAS were the same at the strongest aberration value, even though MV had 5 dB more contrast at 0

Table XVII: Characterization of estimated profile for the tissue aberrator B.

Method	Aberration strength(ns)	correlation length (mm)
ML	45 ± 9.7	7.2 ± 1.1
SCM	68 ± 20.0	6.0 ± 1.9
Rigby	63 ± 25.3	5.9 ± 1.4

Table XVIII: Contrast (in dB) for the experimental cyst target at 40 mm depth and 0 mm lateral position with tissue aberrator A and B. The percent change from the no aberration case is shown in parentheses.

	Contrast(dB)		
Aberration strength	**Control**	**Aberrator A**	**Aberrator B**
DAS	17.3	14.1 (-19%)	8.9 (-49%)
DAS + ML	17.3	15.6 (-10%)	13.6 (-21%)
DAS + SCM	17.3	16.5 (-4%)	9.2 (-47%)
DAS + Rigby	17.3	16 (-8%)	11.3 (-34%)
MV	24.0	15.3 (-36%)	8.5 (-65%)
MV + ML	24.0	17.5 (-27%)	15 (-38%)
MV + SCM	24.0	17.4 (-27%)	9.5 (-60%)
MV + Rigby	24.0	17.1 (-29%)	12.0 (-50%)
ESMV (1%)	29.4	22.6 (-23%)	11.3 (-62%)
ESMV (10%)	25.9	19.3 (-26%)	9.5 (-63%)

Table XIX: Contrast-to-noise ratio for the experimental cyst target at 40 mm depth and 0 mm lateral position with tissue aberrator A and B. The percent change from the no aberration case is shown in parentheses.

	CNR		
Aberration strength	**Control**	**Aberrator A**	**Aberrator B**
DAS	2.17	2.25 (3.6%)	1.58 (-27%)
DAS + ML	2.17	2.42 (11.4%)	1.98 (-9%)
DAS + SCM	2.17	2.51 (15.5%)	1.57 (-28%)
DAS + Rigby	2.17	2.46 (13.3%)	1.80 (-17%)
MV	2.49	2.38 (-4.5%)	1.41 (-43%)
MV + ML	2.49	2.27 (-8.8%)	2.24 (-10%)
MV + SCM	2.49	2.35 (-5.7%)	1.66 (-33%)
MV + Rigby	2.49	2.34 (-6.2%)	2.03 (-19%)
ESMV (1%)	2.13	2.35 (10.0%)	1.38 (-35%)
ESMV (10%)	2.10	2.26 (7.9%)	1.29 (-38%)

ns. ESMV showed a little more robustness than regular MV at low aberration values. However, this algorithm breaks down at 40 ns, and by 60 ns its degradation was equivalent (or even worse) than that suffered by conventional MV.

Similar trends can be inferred from the experiments with electronic aberration. ESMV again showed better contrast at low aberration values (about 1 dB higher) but its degradation at 40 and 60 ns was comparable to that of conventional MV. For these experimentes, the CNR values showed a slightly peculiar behavior at low aberration values, where in some cases aberration caused the CNR to increase. The explanation for this is that aberrated images seem to have brighter speckle due to speckle smearing, which reduces the variance of the background [15].

For the case of the tissue-based aberrator, MV exhibited again higher degradation of contrast when compared to DAS on both cysts. It is noted that even though the estimated aberration was around 20 ns for aberrator A, the effects seemed much worse than the corresponding case in electronic aberration. This can be attributed to the fact that in tissue, other degrading effects are present (diffuse reverberation

Table XX: Contrast (in dB) for the experimental cyst target at 40 mm depth and 10 mm lateral position with tissue aberrator A and B. The percent change from the no aberration case is shown in parentheses.

	Contrast(dB)		
Aberration strength	**Control**	**Aberrator A**	**Aberrator B**
DAS	19.0	15.5 (-19%)	15.6 (-18%)
DAS + ML	19.0	18.1 (-5%)	18.6 (-2%)
DAS + SCM	19.0	17 (-10%)	16.4 (-14%)
DAS + Rigby	19.0	16.2 (-15%)	16.7 (-12%)
MV	25.7	17.8 (-31%)	14.8 (-42%)
MV + ML	25.7	20.4 (-21%)	18 (-30%)
MV + SCM	25.7	21.5 (-16%)	16.6 (-36%)
MV + Rigby	25.7	20.6 (-20%)	17.3 (-33%)
ESMV (1%)	38.7	39.4 (2%)	20 (-48%)
ESMV (10%)	32.7	18.6 (-43%)	17.2 (-48%)

Table XXI: Contrast-to-noise ratio for the experimental cyst target at 40 mm depth and 10 mm lateral position with tissue aberrator A and B. The percent change from the no aberration case is shown in parentheses.

	CNR		
Aberration strength	**Control**	**Aberrator A**	**Aberrator B**
DAS	2.48	2.44 (-1.5%)	2.42 (-2%)
DAS + ML	2.48	2.46 (-0.9%)	2.74 (11%)
DAS + SCM	2.48	2.52 (1.6%)	2.24 (-9%)
DAS + Rigby	2.48	2.61 (5.2%)	2.86 (16%)
MV	2.27	1.93 (-15.0%)	2.31 (2%)
MV + ML	2.27	1.97 (-13.2%)	2.57 (13%)
MV + SCM	2.27	1.94 (-14.3%)	2.77 (22%)
MV + Rigby	2.27	2.07 (-8.9%)	2.65 (17%)
ESMV (1%)	1.99	1.82 (-8.6%)	2.18 (9%)
ESMV (10%)	1.96	1.61 (-17.9%)	2.09 (7%)

[16] and lower SNR due to the attenuation of the tissue). For both aberrators, the degradation of ESMV was slightly lower.

These results suggest that in the presence of a moderate or strong aberrator, the performance gain of MV is completely lost and is no better than DAS. Additionally, although ESMV can show a better degree of robustness at low aberrations, at higher aberration values it is no better than conventional MV and thus its robustness improvement is limited. ESMV also showed "black box" artifacts where speckle disappears in some zones of the image [4]. The artifact is especially noticeable around bright point targets as shown in Figure 4.

2.3.2 Effects of phase aberration correction

The simulations and experimental data presented here show that basic PAC methods are useful in decreasing the detrimental effects of phase aberrations on the MV beamformer. It is observed that the ML

method produced the estimation with lowest mean absolute error. This observation is statistically significant for the simulations at 20 ns (p-value < 0.02) and for all the electronic aberration cases (p-value < 0.001) but not for the 40 and 60 ns simulation cases (p-value > 0.08). The error in the estimation for point targets was slightly lower than for cyst targets because of the high coherence of the point target. Additionally, the obtained errors are consistent with the literature [17].

In terms of image quality and metrics, the ML method tended to outperform the other two methods in correcting the images for the the cyst target simulations and experiments. There are two possible reasons for this situation. First, by estimating the delays through a least-squares inverse problem, ML can produce estimated profiles that are fitted in a global way to every element. The other reason is that in speckle based targets there exists a fundamental spatial decorrelation predicted by the Van Cittert–Zernike theorem and so distant elements in the aperture show little to no correlation. As ML only takes a limited number of channel lags in forming the system of equations, it is less sensitive to this decorrelation of distant elements. In accordance with these observations, the following discussion will focus on the results with ML as it is the PAC method that carried the best improvements overall.

In contrast with the higher sensitivity of MV, PAC methods applied before beamforming showed a greater impact on MV than in DAS, mitigating considerably the deleterious effects of aberration. For example, in the results for the simulations the gains after application of ML on the MV were six times (in FWHM) and two times (in PSL) the gains obtained for DAS. These improvements allowed the MV+ML beamformer to outperform DAS in the case of higher aberration in all metrics: gains of 0.5 mm in FWHM, 17 dB in PSL, 7 dB in contrast and 0.3 in CNR. The performance of the ESMV was more robust than that of conventional MV at low aberrations but at medium to high aberrations MV+ML was better by around 0.6 mm in FWHM, 30 dB in PSL, 20 dB in contrast and 1.1 in CNR.

Similar results are obtained for case of electronic aberration in phantom experiments. The trends present int the simulations are the same, but the improvements have a lower magnitude. This can be explained in the fact that experiments presented other degradation sources, such as noise, and that, while simulations consisted on a single point target, experimental phantoms consisted of a point target embedded in speckle. As observed on the results section, the improvements obtained with DAS allowed the MV+ML beamformer to outperform DAS in FWHM (by 0.15 - 0.20 mm), PSL (by 3 dB), constrast (by 3 dB) and CNR (by 0.25) and also ESMV in these four metrics (by 0.03 - 0.20 mm in FWHM, by 18 dB in PSL, by 16 dB in contrast and by 2.4 in CNR at the highest aberration value).

Similarly, improvements of up to 3 dB were obtained with PAC in DAS and MV for cyst targets with aberrator A. MV+PAC had a contrast that was about 2 dB higher when compared to DAS. At this aberration strength (estimated at around 20 ns), ESMV is still a viable option, having around 4-20 dB more contrast. The reduction in the effects of PAC in both DAS and MV are attributed to the other degrading effects, i.e. reverberation and low SNR. These effects not only degrade the quality of the images but also produce a less accurate estimation of profiles. For the aberrator B case (around 45 ns), the results are consistent with those obtained for simulations and electronic aberration in the sense that ESMV started to break down and MV+PAC was a better option at this moderate-high aberration value. MV+PAC has around 1.4 dB higher contrast 0.25 higher CNR than DAS+PAC and is also superior to ESMV by 3 dB in contrast 0.8 in CNR for the central cyst. The contrast of ESMV with $\beta = 1\%$ in the cyst at 10 mm lateral position was higher than MV+PAC by around 2 dB but the CNR is lower by 0.4. Additionally, due to the artifacts that appear in the ESMV images at this aberration strengths, MV+PAC might be preferable in these situations.

In summary, the use of PAC methods (particularly ML) showed both qualitative and quantitative enhancements on both DAS and MV for different aberration levels. However, the biggest effects were observed for MV. The combination of MV+ML improved results with respect to DAS+ML in lateral resolution, PSL and contrast. Additionally, ESMV is a viable option for low aberration levels, especially due to its improved contrast. However, the simulations and experimental data show that at moderate and high levels of aberration it degrades quickly and MV with PAC shows better performance and less artifacts.

It should also be noted that, although correction was only performed on reception, the images showed quantitative and qualitative recoveries. However, a scheme with correction on both transmission and reception should produce better improvements. This analysis demonstrates the impact of clinic strength aberrator on the MV beamformer, as PAC methods have shown to work for experimental data corrupted with aberration values of up to 60 ns, which are values normally encountered in the human body [18]. Indeed, PAC is necessary for *in vivo* imaging with MV because it is sensitive to even small second order aberrations. All of these methods are based on the assumption of a phase screen model and therefore this precorrection step is limited in its adaptive correction capability. Despite this situation, some modest improvements (around 1-2 dB) were obtained with the tissue-based aberrators (which are distributed aberrators). Further analysis should be considered as a locally adaptive correction method integrated into the MV beamformer will be needed for stronger distributed aberrators and *in vivo* situations.

Chapter 3

Part II: Proposed LAPAC method

3.1 LAPAC Beamformers

3.1.1 Iterative aberration correction in synthetic aperture data

Iterative aberration correction normally consists on estimating the aberration profile in reception and then using this profile to correct the transmission focus and re-fire the whole sequence [19]. However, by using synthetic aperture data the correction in transmission can be performed by the appropriate delays applied to each transmission index instead of having to refire an acquisition sequence again. The channel data is first focused on reception. The compounding is necessary to yield high spatial correlation from the speckle signals. These estimations are performed in the transmission aperture, due to acoustic reciprocity [20]. The aberration profiles are estimated using a certain numbers iterations by repeatedly correcting on reception only and estimating on transmission, i.e. after a first estimation of the aberration profiles is obtained, it is used to correct on reception only (thus improving the reception focus and the exploitable correlation between channels), then a second estimation of the aberration in transmission is performed and this estimation is is used to correct again in reception, with this process iterated four times. The final correction is performed on reception and transmission. It is noted that, due to computational reasons, all the iterative estimation process is implemented in the frequency domain.

3.1.2 Estimation of the aberration profile

The method used for the estimation of the aberration profiles is a hybrid method that combines the scaled covariance matrix (SCM) formulation [12] and the multilag (ML) least squares algorithm [21, 22]. This new method, from here on referred as SCM-ML method, was developed as original ML needs a high sampling rate and is computationally expensive, while the original SCM formulation is fast and convenient but its performance is inferior to that of ML as shown in the previous chapter. The method uses the estimated covariance matrix $R = [R(m,n)]$ of the data compounded on reception. Following the formulation by Silverstein and Ceperley [12], each entry of the covariance matrix can be expressed as

$$R(m,n) \cong |R(m,n)| e^{j[\phi(m)-\phi(n)]}, \tag{1}$$

where $\phi(m)$ is the corrupting phase for channel m, and thus, the phase of $R(m,n)$ correspond to the relative phase difference between channels m and n. Accordingly, the relative phases of channels separated up to a certain lag M correspond to the phase of the elements of the M first off-diagonals of the covariance matrix. Using the phase closure property, an overdetermined system of equations can be casted as in conventional ML [10] but using the phase differences instead of the time shifts obtained from correlations. The system is solved using the method of least squares and the time delays are determined. The obtained profile is used to correct in transmission and reception the channel data by multiplying element-wise the Fourier transform $\mathcal{F}(\omega)$ of the channel data window ω described in 3.1.5 with an array of phase shifts $\Phi(f,m,k) = \exp[\mathrm{j}2\pi f(\mathcal{P}(m)+\mathcal{P}(k))]$, where $\mathcal{P}(m)$ is the estimated aberrant phase for the m-th element, f is the discrete frequency value, m is the receive channel index, and k is the transmit channel index. This multiplication is done before doing the weight calculation and apodization. Note that, for the case of MV, this is mathematically equivalent, although more computationally efficient, to correcting the steering vector $\mathbf{a}$ of a particular frequency bin f_0 with a diagonal the phase matrix $\Psi_{f_0}(m,k) = \Phi(f_0,m,k)$, i.e., a new corrected steering vector is computes as $\bar{\mathbf{a}} = \Psi_{f_0}\mathbf{a}$, or to using this same Ψ_{f_0} for correcting the channel data and the original MV apodization expressed in (3), i.e. applying the corrected weights

$$\bar{\mathbf{w}} = \frac{(\Psi_{f_0}\mathbf{R}\Psi_{f_0}^*)^{-1}\mathbf{a}}{\mathbf{a}^H(\Psi_{f_0}\mathbf{R}\Psi_{f_0}^*)^{-1}\mathbf{a}}, \tag{2}$$

during the apodization stage.

3.1.3 Profile decision logic

For estimation of phase aberration profiles, it is necessary to have high correlation between the different reception (or transmission) channels. According to the van Cittert–Zernike theorem [23], if the imaged zone consists of diffuse scatterers, the normalized spatial covariance is approximated as a triangular function that decreases from 1 at zero lag to 0 at a lag equal to the size of the array. Because ultrasound imaging targets normally consist of diffuse scatterers, it is necessary to have a tight transmission or reception focus in order to have enough correlaation for aberration profile estimation.

However, there exist zones in the image where the signals do not possess enough spatial correlation to estimate a reliable profile (e.g. the areas inside anechoic cysts, where the signals consist mainly on off-axis echoes and noise). To provide a local estimate of the coherence of the channel signals, the short-lag spatial coherence (SLSC) value [24] of the reception-focused data is calculated as a surrogate for the reliability of the profile estimation. SLSC values are obtained for every point in the image domain. Aberration profiles are computed for all points in a region Ω centered around a point (x,z) in the discretized image domain. This size was chosen because it corresponds to the isoplanatic patch size for human tissues [8]. The profiles in Ω that correspond to points whose SLSC values is below a certain threshold are discarded, and the remaining profiles are averaged to obtain a final profile. However, if one of those given regions Ω has less than a certain percentage of usable profiles, the final profile from the whole region Ω is discarded and the latest previously computed profile for that particular lateral position is utilized.

3.1.4 Conventional MV beamformer

The standard MV beamformer seeks to find, for each point, the apodization that minimizes the variance of the beamformed output signal while maintaining a unitary gain in the presumed direction of arrival. This is done by computing the optimal weights $\mathbf{w}$ that satisfy [2]

$$\mathbf{w} = \frac{\mathbf{R}^{-1}\mathbf{a}}{\mathbf{a}^H\mathbf{R}^{-1}\mathbf{a}}, \tag{3}$$

where $\mathbf{R}$ is the spatial covariance matrix of the signals received at the different array elements and $\mathbf{a}$ is the steering vector. If signals are first pre-steered, as is necessary for the broadband signals in ultrasound imaging, $\mathbf{a}$ reduces to a vector of ones. To take into account the coherence of the signal and handle ill conditioning of the spatial covariance matrix, spatial smoothing is used [2]. Spatial smoothing divides the array channel data into subarrays of size L and averages the covariance matrices of each subarray.

Holfort *et al.* [1] adapted the minimum variance beamformer to the frequency domain by calculating the Fourier transform of continuous axial windows and applying the MV beamformer to each of the frequency bins. Weight calculation for each frequency bin also uses spatial smoothing in the computation of the covariance matrix. A beamformed value is obtained for each frequency bin and thus a complete beamformed spectrum is obtain. The inverse Fourier transform of this spectrum is obtained and the center value of the resulting time domain signal is the final value of that particular point. The proposed method is based on this beamformer because the subdivision into narrowband beamformers allow the application of phase shifts to correct the signals during the beamforming process. Hereby, this approach will be referred to as conventional MV.

3.1.5 Proposed LAPAC beamformer

The method requires multistastic synthetic aperture data. For each point (x,z) in the discretized image domain, the channel data is focused on transmission and reception at (x,z) and a window of $\omega(n,m,k)$ cented at this point is obtained from the multistastic channel data. Here, the axial dimension index is given by $n = z-W,\ldots,z+W$, where $2W+1$ is the window axial length, the receive element index is given by $m = 1,\ldots,M$, where M is the number of channels, and the transmission element index is given by $k = 1,\ldots,M$. The analytic channel signals corresponding to window W are then coherently compounded in reception in order to synthetically form a receive beam, i.e. $C(n,k) = \sum_m W(n,m,k)$. $C(n,k)$ is used to estimate both the aberration profile in transmission and a short-lag spatial coherence (SLSC) value, which is used for profile decision logic (Section 3.1.3). The aberration is done in an iterative fashion as explained in Section 3.1.3, and after a final correction profile is obtained for the current point, the original window of channel data, is corrected in the frequency domain in both transmission and reception. The final beamformed value is obtained from W by either the DAS or the MV beamformer.

The general scheme of the Locally Adaptive Phase Aberration Correction (LAPAC) beamformer is shown in Figure 8. The additional blocks corresponding to LAPAC, i.e. local PAC estimator, correction of signals and SLSC-based decision logic, are shown with a solid blue border.

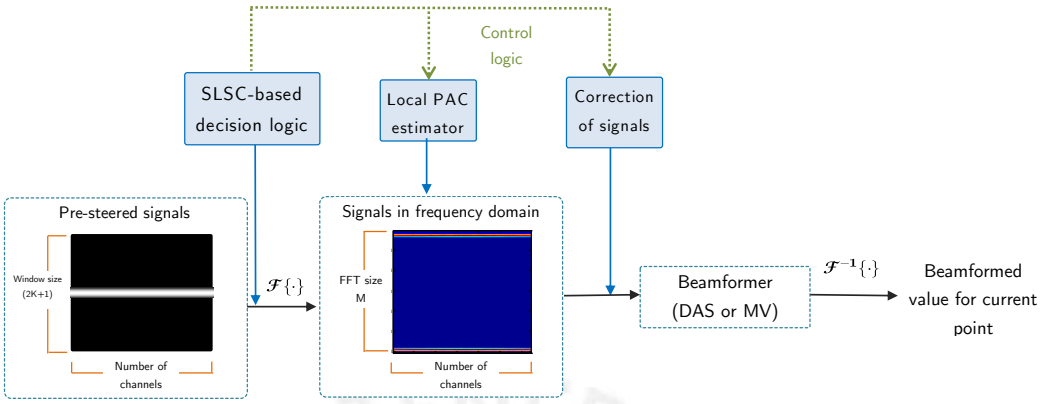

Figure 8: General scheme of the proposed beamformer. The blocks corresponding to estimation and correction used in LAPAC are shown with a solid blue border and light blue background

3.2 Methods

3.2.1 Fullwave simulations

Two isoimpedance simulations were generated using a full wave simulator [25]. An isoimpedance simulation is one where the impedance map is constant and thus reverberation effects are supressed. The isoimpedance simulations allowed direct calculation of aberration without confounding effects of reverberation for this study analysis. In order to generate isoimpedance data, simulations of the phantom with the aberrator and for the aberrator alone are performed. Afterwards, the aberrator alone RF data were subtracted from the phantom with the aberrator RF data in order to eliminate reverberation effects and isolate the RF dataa with phase aberration. For each simulation, a different human abdominal wall model [26] was placed between the transducer and the phantoms. The first model was a 22 mm thick abdominal wall and the second model was a 25 mm thick abdominal wall. These two abdominal aberrator models will be referred as aberrators A and B, respectively. In both simulation sets, the phantom consisted of four 2.2 mm radius anechoic cyst targets located at axial depths of 45, 50, 55 and 60 mm for aberrator A, and 40, 45, 50 and 55 mm for aberrator B, and at -5 mm and 5 mm lateral positions. Four different realizations of the speckle map were simulated for each dataset and multistastic synthetic aperture data was recorded. Matched simulations with no tissue were also generated in order to produce control data. The simulated array consisted of 128 elements with a central frequency of 5 MHz and a sampling frequency of 40 MHz.

3.2.2 Experiments with tissue aberrators

Channel data was acquired using a multistastic synthetic aperture sequence and a multipurpose phantom model 539 (ATS Laboratories, Connecticut, USA) using a Verasonics V1 acquisition system (Verasonics Inc, Washington, USA). A 128 element L11-4V linear transducer with a central frequency of 5 MHc was used and the data was sampled at 20 MHz, which was interpolated to 40 MHz offline. The phantom

consisted of three 2 mm radius cysts separated by 10 mm axially. A 28 mm section of beef loin was used placed between the transducer and the phantom in order to induce aberration.

3.2.3 In vivo experiments

The same experimental parameters and data acquisition sequence described in the previous section were used to obtain channel data from a cross section of the internal (ICA) and external carotid arteries (ECA) of a 24-year-old healthy male volunteer. Written informed consent was obtained before performing the scan.

3.2.4 Comparisons and metrics

The proposed LAPAC-MV and LAPAC-DAS methods are compared on all datasets with DAS, precorrected DAS (DAS-PC, i.e. a precalculated profile is applied for each lateral position before applying DAS beamforming), conventional MV and precorrected MV (MV-PC, i.e. a precalculated profile is applied for each lateral position before applying conventional MV beamforming). All DAS, MV and LAPAC-MV images were reconstructed on a rectangular grid of 0.08 mm lateral spacing and 0.03 mm axial spacing. For MV-based beamformers, the length of the axial window was 121 samples, the FFT was performed using 128 frequency bins and the spatial smoothing parameters was 32. For the aberration correction, the region Ω had a size equal to 0.4 mm $\times$ 0.4 mm. This size was chosen because it corresponds to the isoplanatic patch size for human tissues [8]. Four iterations were used for the iterative procedure. For LAPAC-MV, the SLSC was computed using 30 lags, i.e. 23% of the aperture size, and a threshold value of 6 was used (These values are consistent with the values uses in SLSC imaging [24, 27]). The percentage threshold under which the profile of a region Ω is discarded was set to 25 %.

In the DAS and MV precorrected cases, PAC is applied as it is typically done in the literature [8]; profiles corresponding to each lateral position and a number of axial positions below and above a user-selected depth are computed before the beamforming process. The profiles were obtained using four iterations of the SCM-ML method. The profiles are averaged laterally and axially within the same isoplanatic patch sizes uses for LAPAC-DAS and LAPAC-MV the final profiles are applied on both transmission and reception in the time-domain before the beamforming process. The beamforming methods are compared in terms of contrast and contrast-to-noise ratio (CNR) defined by

$$\text{Contrast} = 20\log\left(\frac{\mu_1}{\mu_0}\right)$$

$$\text{CNR} = \frac{|\mu_1 - \mu_0|}{\sqrt{0.5(\sigma_1^2 + \sigma_0^2)}},$$

where μ_1 and μ_0 are the mean values of the region of interest (ROI) and background, respectively, and σ_1^2 and σ_0^2 are the variances of the ROI and the background, respectively.

Additionally, some computational times are presented for DAS, MV and LAPAC-MV. All tests were performed using a standard portable computer with a Intel core i7 processor and 8 Gb of RAM.

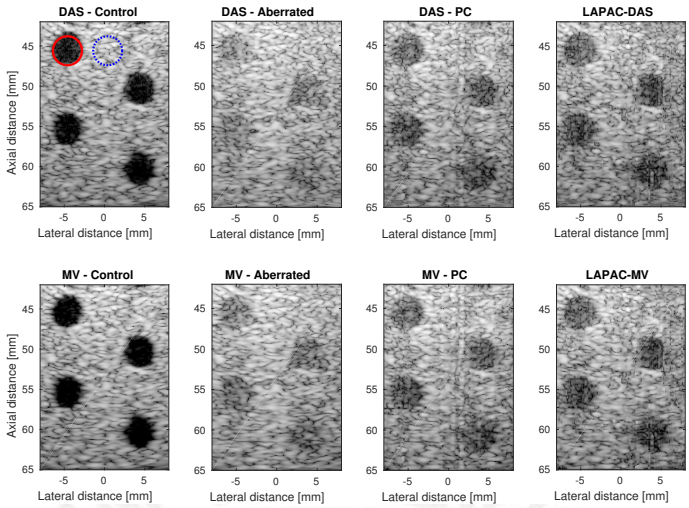

Figure 9: B-mode images of the simulated cyst targets with aberrator A and with different beamforming methods. On the first image, an example of a ROI image (red) and a background region (blue) used for the calculation of metrics are shown.

Table XXII: Contrast (in dB) for the fullwave simulations with aberrator A and aberrator B and different beamforming methods with and without aberration calculated at the cyst targets at different depths.

	Aberrator A				**Aberrator B**			
	Cyst depth (mm)				**Cyst depth (mm)**			
	45	**50**	**55**	**60**	**40**	**45**	**50**	**55**
DAS – Control	16.8 ± 3.3	16.2 ± 2.5	15.1 ± 4.3	15.3 ± 3.6	28.4 ± 1.2	27.9 ± 0.9	26.5 ± 0.7	27.4 ± 0.2
DAS – Aberrated	8.7 ± 0.1	7.6 ± 1.6	8.4 ± 0.5	6.9 ± 0.3	8.1 ± 1.3	9.7 ± 0.7	7.0 ± 1.2	11.2 ± 0.6
DAS – PC	11.8 ± 1.3	9.1 ± 2.2	10.9 ± 0.9	8.3 ± 1.4	13.9 ± 1.9	12.3 ± 1.4	13.2 ± 1.9	11.7 ± 1.5
LAPAC – DAS	12.7 ± 0.8	10.6 ± 2.5	13.6 ± 0.7	9.5 ± 1.2	14.2 ± 2.4	13.4 ± 1.7	12.6 ± 2.2	13.1 ± 2.4
MV – Control	16.2 ± 2.4	15.5 ± 3.1	14.4 ± 3.5	14.1 ± 3.0	33.5 ± 0.0	32.1 ± 1.0	30.1 ± 0.6	29.4 ± 0.2
MV – Aberrated	10.5 ± 0.3	9.3 ± 1.6	9.5 ± 0.6	8.8 ± 0.4	9.9 ± 1.8	11.6 ± 0.6	8.6 ± 1.3	13.5 ± 0.7
MV – PC	12.1 ± 0.8	9.4 ± 1.6	11.6 ± 1.2	8.8 ± 1.1	14.7 ± 2.4	14.1 ± 1.7	14.5 ± 1.8	13.9 ± 1.5
LAPAC – MV	13.3 ± 1.1	11.2 ± 2.6	13.4 ± .8	10.6 ± 1.4	15.9 ± 2.5	15.2 ± 1.7	14.5 ± 2.5	15.0 ± 2.9

3.3 Results

3.3.1 Fullwave Simulations

B-mode images of one the realizations of the full-wave cyst target simulations with the different beamforming methods are shown in Figure 9 for aberrator A and in Figure 10 for aberrator B (All images are displayed with a dynamic range of 50 dB). Control images with no aberration are included for comparison. Circular regions of 2 mm radius corresponding to the cysts and background were used for all cyst targets in order to compute contrast and CNR. An example of these regions is shown in the first image of figure 9 and the average and standard deviation of the metrics for the four realizations are displayed in Tables XXII and XXIII.

It is observed that aberration degrades the contrast of both DAS and MV by approximately 5-8 dB and the CNR by approximately 0.1-0.5 for aberrator A. The degradation is higher with aberrator B, with losses of 16-24 dB or more in contrast and 0.1-0.5 in CNR. Accordingly, the cysts are difficult to distinguish in any of the aberrated images. For aberrator A, the application of precorrection increases

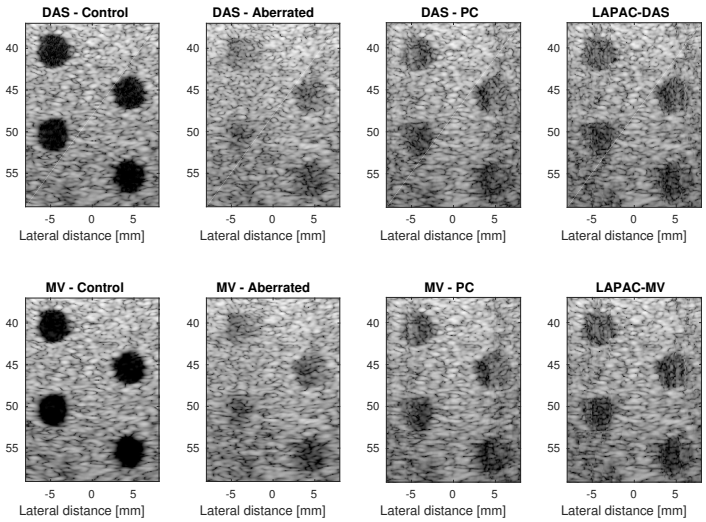

Figure 10: B-mode images of the simulated cyst targets with aberrator B and with different beamforming methods. On the first image, an example of a ROI image (red) and a background region (blue) used for the calculation of metrics are shown.

Table XXIII: CNR for the fullwave simulations with aberrator A and aberrator B and different beamforming methods with and without aberration calculated at the cyst targets at different depths.

	Aberrator A				**Aberrator B**			
	Cyst depth (mm)				**Cyst depth (mm)**			
	45	**50**	**55**	**60**	**40**	**45**	**50**	**55**
DAS – Control	1.25 ± 0.21	1.42 ± 0.21	1.35 ± 0.36	1.42 ± 0.25	1.52 ± 0.06	1.55 ± 0.15	1.59 ± 0.03	1.79 ± 0.04
DAS – Aberrated	1.04 ± 0.06	1.06 ± 0.22	1.07 ± 0.08	$.91 \pm 0.05$	0.99 ± 0.09	1.20 ± 0.08	0.90 ± 0.11	1.37 ± 0.06
DAS – PC	1.14 ± 0.16	1.10 ± 0.22	1.24 ± 0.15	$.94 \pm 0.14$	1.29 ± 0.10	1.34 ± 0.15	1.37 ± 0.19	1.35 ± 0.17
LAPAC – DAS	1.13 ± 0.08	1.16 ± 0.24	1.28 ± 0.13	1.03 ± 0.13	1.29 ± 0.13	1.35 ± 0.08	1.27 ± 0.18	1.36 ± 0.14
MV – Control	1.23 ± 0.14	1.38 ± 0.28	1.31 ± 0.25	1.34 ± 0.22	1.57 ± 0.07	1.59 ± 0.20	1.60 ± 0.01	1.80 ± 0.06
MV – Aberrated	1.16 ± 0.07	1.26 ± 0.18	1.14 ± 0.14	1.09 ± 0.07	1.13 ± 0.15	1.33 ± 0.08	1.02 ± 0.12	1.47 ± 0.12
MV – PC	1.15 ± 0.13	1.18 ± 0.16	1.27 ± 0.14	1.01 ± 0.09	1.34 ± 0.15	1.42 ± 0.17	1.40 ± 0.18	1.49 ± 0.14
LAPAC – MV	1.18 ± 0.10	1.23 ± 0.26	1.26 ± 0.19	1.11 ± 0.15	1.36 ± 0.14	1.45 ± 0.14	1.36 ± 0.15	1.46 ± 0.09

contrast by 2-3 dB for DAS and 0.1-2 dB for MV, and CNR by 0.01-0.2 for DAS, but it does not increase, or even lowers, the CNR in MV. On the other hand, both LAPAC-DAS and LAPAC-MV show increments of 2-3 dB in contrast and 0.04-0.15 with respect to the uncorrected case. In accordance with the highest degradation with aberrator B, higher improvements are also obtained with the correction. Precorrection increases 3-6 dB in contrast for both DAS and MV, while LAPAC-DAS and LAPAC-MV show increases of 4-6 dB in contrast. The time in seconds needed to calculate a point in the image domain is shown in XXIV. It is noted that LAPAC-MV takes more than twice the time of MV and is more than three orders of magnitude slower than DAS.

Table XXIV: Time in seconds for the calculation of a point with the different beamforming methods

	DAS	**MV**	**LAPAC-MV**
Average Time (seconds)	0.004352	7.1	16.248

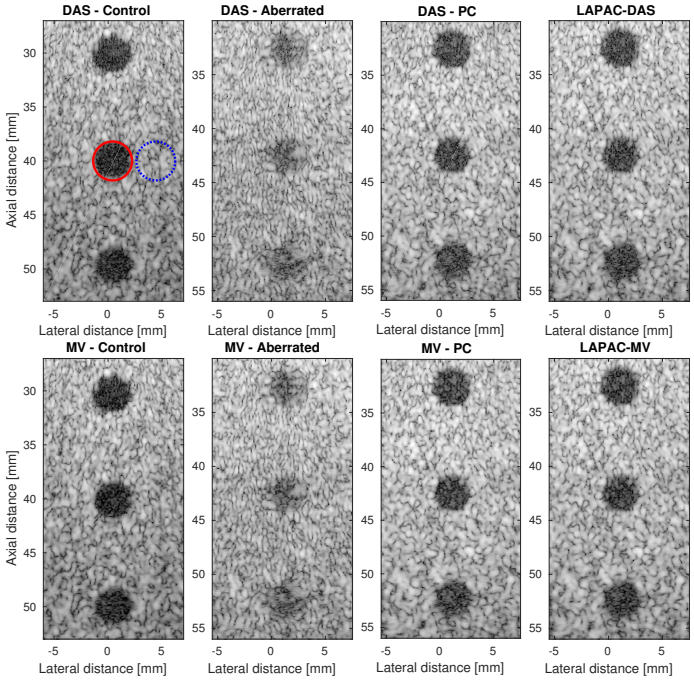

Figure 11: B-mode images of the experimental cyst target and tissue aberrator with different beamforming methods. On the first image, an example of a ROI image (red) and a background region (blue) used for the calculation of metrics are shown.

3.3.2 Tissue Aberrator

B-mode images of the experimental cyst targets with the physical aberrator with the different beamforming methods are shown in Figure 11. Control images with no aberration are included for comparison but do not have a direct match to the aberrated corrected images due to the removal of the aberrating tissue and the subsequent repositioning of the transducer. Circular regions of 1.8 mm radius corresponding to the cysts and background were used for all cyst targets in order to compute contrast and CNR. These metrics are shown in Table XXV.

It is observed that aberration degrades the contrast of both DAS and MV by approximately 6-10 dB and the CNR by approximately 0.4-0.5. The quality of the cysts as well as the texture of the speckle background are greatly degraded. The application of precorrection increases contrast by 6-7 dB in both DAS and MV. Both LAPAC methods increases contrast by 7-9 dB compared to the uncorrected case.

3.3.3 Results of in vivo carotid

B-mode images of the *in vivo* images with the different beamforming methods are shown in Figure 12. Circular regions of 1.5 mm radius inside the ECA and ICA and in the sorrounding tissue where selected to compute contrast and CNR. These metrics are shown in Tables XXVI.

It can be observed that both the ICA and ECA present some clutter inside. In this case, the application of classical precorrection does not improve much the quality of the images. However, it is

Table XXV: Contrast and CNR of the experimental cyst target and tissue aberrator with different beamforming methods

	Contrast (dB)			CNR		
	Cyst depth (mm)			Cyst depth (mm)		
	45	**50**	**55**	**45**	**50**	**55**
DAS – Control	18.8	18.2	13.8	1.58	1.65	1.33
DAS – Aberrated	10.0	8.6	7.6	1.17	1.07	0.97
DAS – PC	17.0	16.2	13.1	1.59	1.60	1.41
LAPAC – DAS	19.4	16.0	14.5	1.62	1.63	1.42
MV – Control	20.3	17.8	14.1	1.60	1.60	1.37
MV – Aberrated	10.4	8.6	7.7	1.18	1.07	0.98
MV – PC	17.7	16.3	13.2	1.63	1.64	1.41
LAPAC – MV	19.7	16.4	14.6	1.63	1.67	1.44

Table XXVI: Contrast and CNR of the in vivo carotid image with different beamforming methods

	Contrast (dB)		CNR	
	ECA	**ICA**	**ECA**	**ICA**
DAS – Aberrated	20.0	24.8	1.74	1.74
DAS – PC	19.4	24.4	1.74	1.74
LAPAC – DAS	20.9	25.9	1.45	1.45
MV – Aberrated	22.7	27.8	1.8	1.8
MV – PC	21.6	27.3	1.8	1.8
LAPAC – MV	24.3	29.1	1.49	1.49

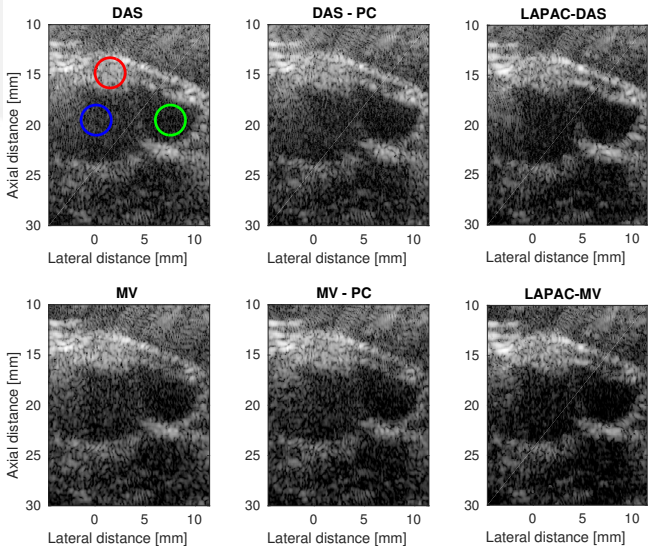

Figure 12: B-mode images of the *in vivo* carotid with different beamforming methods. The blue and green circles represent the regions taken inside the ECA and ICA. The red circle is the one taken in the sorrounding tissue and considered as background.

observed that LAPAC-DAS does show some improvement (around 1 dB) with respect to the uncompensated case and LAPAC-MV presents contrast 2-3 dB higher than all the other methods. Although the CNR decreases for both LAPAC methods, the images look visually enhanced.

3.4 Discusion

As seen in the previous chapter, it is noted that after the application of a moderate or strong aberrator, the performance of MV is comparable to that of DAS. The results of the fullwave simulation show that common precorrection can improve the contrast of MV by around 2 dB but LAPAC-DAS and LAPAC-MV had on average 1.5-3 dB higher contrast than their precorrected counterparts, and thus conveyed increases of around 3-6 dB with respect to the uncorrected case. The enhanced performance of LAPAC is especially noticeable for the rightmost cysts in Figure 9. Aside from having a better contrast on average, it should be noted that LAPAC-MV showed better contrast than all the other methods for all realizations and cyst depths. Overall, LAPAC-MV benefited more from the adaptive correction and showed higher contrast than LAPAC-DAS for almost all cases.

However, the CNR values of the LAPAC methods are comparable to PC because LAPAC-DAS and LAPAC-MV had a higher variance in the background that might be caused for the variance of the profiles applied in the continuous correction. The variance of the applied profiles can be diminished by averaging profiles on a larger region thought this may incur in a higher bias. In any situation, the size of the averaging region cannot be enlarged too much as it has to respect the isoplanatic patch size [22].

The same trends are observed in the tissue aberrator results. With the tissue aberrator, the contrast and visibility of the cysts in both MV and DAS images are greatly reduced. Precorrection increases contrast in both DAS and MV by about 7 dB. The higher impact of precorrection compared to the fullwave simulations might be due to the different configuration of the tissue layers that make the physical aberrator be closer to a near field phase screen than the tissue used for simulations. LAPAC-DAS and LAPAC-MV presented contrast values that were around 2 dB higher than MV-PC. In this case, these two methods perform almost equivalently.

Additionally, the *in vivo* results of the carotid suggest that LAPAC-MV might be of clinical importance, augmenting the contrast and edge definition of certain regions. While DAS-PC and MV-PC do not improve contrast or CNR, LAPAC methods increase contrast by 2-3 dB in both the ECA and ICA. LAPAC-MV shows 4 dB higher contrast than LAPAC-DAS and enhancements are noticeable inside the ICA, where less clutter is present. Although there are contrast and visual improvements, the CNR metric goes down in LAPAC methods due to the variance that may be caused in the tissue zone. This can be partially be caused by the small region that has to be selected for the CNR calculation due to the size of the sorrounding tissue.

The improved performance of LAPAC stems from two particular reasons. First, correction is adaptive and is performed continuosly over the image domain, while normal precorrection assumes an infinite isoplanatic axial extension, i.e. a single profile is used for the whole lateral position. The design of LAPAC-MV allows it to seamlessly integrate the correction to all axial positions by using a synthetic aperture sequence and acoustic reciprocity. Second, the logic of the profiles to apply at any given point are based on a quantitative measure, e.g., SLSC, instead of a manually selected depth that may depend on the expertise of the user, as is the case of normal precorrection.

Although LAPAC-MV has not yet been tested against other robust MV beamformers present in the literature, results of the previous chapter showed that MV-PC can be a preferable alternative to other robust MV beamformers in the presence of moderate-strong aberrators and distributed aberrator. As we have shown here that LAPAC-MV showed increased performance when compared to MV-PC, it is considered that LAPAC-MV might be a preferable option when compared to previous robust MV beamformers.

It should be noted that the tissue aberrator and *in vivo* experiments present other degrading effects aside from aberration, i.e., reverberation and reduced signal-to-noise ratio, which were not present in the isoimpedance simulations. These affect the quality of the image and create bias and jitter in the aberration estimation. Therefore, the enhancements obtained with precorrection and the LAPAC method in experimental datasets is lower than that of fullwave simulations. The presence of reverberation will also degrade MV performance and push it toward DAS beamforming. To solve this problem, the MV might be combined with reverberation clutter filters such as ADMIRE [28] or F-X[29] or direction of arrival filters [30].

Although there are some artifacts present in the simulation images, the correct performance of the algorithm in the different tested dataset suggest that the SLSC value is a good measure of realiability of profiles, allowing LAPAC to automatically determine if signal coherence is high enough to compute the aberration profile and adjust the beamformer accordingly without operator intervention. A key advantage of SLSC values is that it is a normalized correlation measure and so it is independent of the transmit power, thus making the selection of the thresholds easier and more globally applicable. Other coherence measures such as the generalized coherence factor (GCF) [31] or the phase coherence factor (PCF) [32] might also be used to implement the decision logic.

Additionally, it is possible to modify the single-element sequence to other synthetic aperture sequences. In particular, there might be a need to implement other synthetic aperture techniques (e.g. virtual source sequences [33]) for stronger aberrator or other *in vivo* scenarios, where the signal-to-noise ratio of the single element sequence is not sufficient. In fact, it has been shown that is possible to adapt spatial correlation based techniques to this kind of synthetic aperture emissions [27]. It would be straightforward to extend the MV beamformer to these sequences as it only acts on the reception channel data after the data is focused on tranmission and reception and so it is not affected by the actual tranmission sequence. It should also be mentioned that LAPAC has been applied to both DAS and MV but it may be possible to extend it to other adaptive beamforming methods.

A possible concern with the proposed algorithm is that the computational cost of the LAPAC-MV is considerably higher than conventional MV beamformer, as, for each point in the image, it is necessary to perform a calculation of the SLSC value for the descion logic and, in case the decision logic indicates so, an estimation of an aberration profile with a predefined number of iterations. The time of these operations add up to the naturally higher cost associated with the MV beamformer. However, the advent of parallel processing and GPU enabled computing might permit the real-time implementation of the current technique, as there has already been real-time implementations of the conventional MV beamformer [34].

Chapter 4

Conclusions

In the first part of this thesis work, we have shown the effects of different strengths and types of aberration on MV and have compared them with conventional DAS. These results suggest that aberration has a stronger impact on the MV beamformer than previously reported, primarily because previous literature only examined the degradation by gross velocity errors or basic simulated phase screen aberrators. These results suggest that the application of PAC methods is needed to improve the MV beamformer resolution and contrast in clinically relevant scenarios.

The robust MV beamformer tested (ESMV) showed improved robustness at low aberration values but its performance is, in general, no better than that of conventional MV at moderate and high aberrations. MV combined with PAC methods was preferable in these cases. This suggested that the development of a robust MV beamformer algorithm that integrates PAC methods is necessary for clinical use. This situation motivated the work, presented on the second part, where we have presented a new adaptive correction method and showed that it can be applied to both DAS and MV beamformers.

The design of the method permits the estimation of the profiles at all points in the image domain and automatically determines the application of the best profile to apply based on the SLSC value. The tests of the new methods in simulations, experiments with tissue aberrators and *in vivo* carotid images, show that LAPAC-DAS and LAPAC-MV has higher contrast when compared to DAS-PC and MV-PC. Additionally, LAPAC-MV showed on average better performance than LAPAC-DAS. The increased performance of the proposed method with distributed aberrators and the *in vivo* images suggest that LAPAC-MV might be a more clinically viable option to MV-PC to enhance the quality of ultrasonic images.

References

[1] I.K. Holfort, F. Gran, and J.A. Jensen, "Broadband minimum variance beamforming for ultrasound imaging," *Ultrasonics, Ferroelectrics, and Frequency Control, IEEE Transactions on*, vol. 56, no. 2, pp. 314–325, February 2009.

[2] J.-F. Synnevåg, A. Austeng, and S. Holm, "Adaptive beamforming applied to medical ultrasound imaging," *Ultrasonics, Ferroelectrics, and Frequency Control, IEEE Transactions on*, vol. 54, no. 8, pp. 1606–1613, August 2007.

[3] Zhisong Wang, Jian Li, and Renbiao Wu, "Time-delay- and time-reversal-based robust capon beamformers for ultrasound imaging," *Medical Imaging, IEEE Transactions on*, vol. 24, no. 10, pp. 1308–1322, Oct 2005.

[4] S. Mehdizadeh, A. Austeng, T. F. Johansen, and S. Holm, "Eigenspace based minimum variance beamforming applied to ultrasound imaging of acoustically hard tissues," *IEEE Transactions on Medical Imaging*, vol. 31, no. 10, pp. 1912–1921, Oct 2012.

[5] Jian Li, Petre Stoica, and Zhisong Wang, "On robust capon beamforming and diagonal loading," *Signal Processing, IEEE Transactions on*, vol. 51, no. 7, pp. 1702–1715, July 2003.

[6] Xin yuan Xia, Ping Li, Wen tao Wu, and Xiao hui Meng, "Robust minimun variance beamforming applied to ultrasound imaging in the presence of phase aberration," in *Piezoelectricity, Acoustic Waves, and Device Applications (SPAWDA), 2014 Symposium on*, Oct 2014, pp. 122–125.

[7] M.S. Ziksari and B.M. Asl, "Phase aberration correction in minimum variance beamforming of ultrasound imaging," in *Electrical Engineering (ICEE), 2015 23rd Iranian Conference on*, May 2015, pp. 23–26.

[8] J. J. Dahl, M. S. Soo, and G. E. Trahey, "Spatial and temporal aberrator stability for real-time adaptive imaging," *IEEE Transactions on Ultrasonics, Ferroelectrics, and Frequency Control*, vol. 52, no. 9, pp. 1504–1517, Sept 2005.

[9] Liu Dong-Lai and Robert Waag, "Time-shift compensation of ultrasonic pulse focus degradation using least-mean-square error estimates of arrival time," vol. 95, no. January 1994, pp. 542–555, 1993.

[10] R.C. Gauss, M.S. Soo, and G.E. Trahey, "Wavefront distortion measurements in the human breast," in *Ultrasonics Symposium, 1997. Proceedings., 1997 IEEE*, Oct 1997, vol. 2, pp. 1547–1551 vol.2.

[11] K. W. Rigby, "Real-time correction of beamforming time delay errors in abdominal ultrasound imaging," 2000, vol. 3982, pp. 342–353.

[12] S.D. Silverstein and D.P. Ceperley, "Autofocusing in medical ultrasound: the scaled covariance matrix algorithm," *Ultrasonics, Ferroelectrics, and Frequency Control, IEEE Transactions on*, vol. 50, no. 7, pp. 795–804, July 2003.

[13] E. Gonzalez, N. Sheth, B. Castañeda, J. Dahl, and R. Lavarello, "Accuracy of backscatter coefficient estimation in aberrating media using different phase aberration correction strategies - a simulation study," in *Ultrasonics Symposium (IUS), 2014 IEEE International*, Sept 2014, pp. 2438–2441.

[14] Jørgen Arendt Jensen, "Field: A program for simulating ultrasound systems," in *10th Nordicbaltic Conference on Biomedical Imaging, Vol. 4, Supplement 1, Part 1: 351–353*. Citeseer, 1996.

[15] S. A. McAleavey, J. J. Dahl, M. S. Soo, G. F. Pinton, and G. E. Trahey, "Resolution improvement of point targets by real-time phase aberration correction in vivo results," in *Ultrasonics Symposium, 2004 IEEE*, Aug 2004, vol. 1, pp. 235–238 Vol.1.

[16] J. Dahl and N. Sheth, "Reverberation clutter from subcutaneous tissue layers: Simulation and in vivo demostrations," *Ultrasound in Medicine and Biology*, vol. 40, no. 4, pp. 714–726, 2014.

[17] Jeremy J. Dahl and Thomas J. Feehan, "Direction of arrival filters for improved aberration estimation," *Ultrasonic Imaging*, vol. 30, no. 1, pp. 1–20, 2008.

[18] L.M. Hinkelman, T.D. Mast, M.J. Orr, and R.C. Waag, "Effects of abdominal wall morphology on ultrasonic pulse distortion," in *Ultrasonics Symposium, 1997. Proceedings., 1997 IEEE*, Oct 1997, vol. 2, pp. 1493–1496 vol.2.

[19] E. Gonzalez, N. Sheth, B. Castañeda, J. Dahl, and R. Lavarello, "Accuracy of backscatter coefficient estimation in aberrating media using different phase aberration correction strategies - a simulation study," in *Ultrasonics Symposium (IUS), 2014 IEEE International*, Sept 2014, pp. 2438–2441.

[20] N. Bottenus and K. F. Üstüner, "Acoustic reciprocity of spatial coherence in ultrasound imaging," *IEEE Transactions on Ultrasonics, Ferroelectrics, and Frequency Control*, vol. 62, no. 5, pp. 852–861, May 2015.

[21] Dong-Lai Liu and Robert Waag, "Correction of ultrasonic wavefront distortion using backpropagation and a reference waveform method for time-shift compensation," *The Journal of the Acoustical Society of America*, vol. 96, no. 2, pp. 649–660, 1994.

[22] J. J. Dahl, S. A. Mcaleavey, G. F. Pinton, M. S. Soo, and G. E. Trahey, "Adaptive imaging on a diagnostic ultrasound scanner at quasi real-time rates," *IEEE Transactions on Ultrasonics, Ferroelectrics, and Frequency Control*, vol. 53, no. 10, pp. 1832–1843, October 2006.

[23] Raoul Mallart and Mathias Fink, "The van cittert–zernike theorem in pulse echo measurements," *The Journal of the Acoustical Society of America*, vol. 90, no. 5, 1991.

[24] M. A. Lediju, G. E. Trahey, B. C. Byram, and J. J. Dahl, "Short-lag spatial coherence of backscattered echoes: imaging characteristics," *IEEE Transactions on Ultrasonics, Ferroelectrics, and Frequency Control*, vol. 58, no. 7, pp. 1377–1388, July 2011.

[25] G.F. Pinton, G.E. Trahey, and J.J. Dahl, "Sources of image degradation in fundamental and harmonic ultrasound imaging using nonlinear, full-wave simulations," *Ultrasonics, Ferroelectrics, and Frequency Control, IEEE Transactions on*, vol. 58, no. 4, pp. 754–765, April 2011.

[26] T Douglas Mast, Laura M Hinkelman, Michael J Orr, and Robert C Waag, "The effect of abdominal wall morphology on ultrasonic pulse distortion. part ii. simulations," *The Journal of the Acoustical Society of America*, vol. 104, no. 6, pp. 3651–3664, 1998.

[27] N. Bottenus, B. C. Byram, J. J. Dahl, and G. E. Trahey, "Synthetic aperture focusing for short-lag spatial coherence imaging," *IEEE Transactions on Ultrasonics, Ferroelectrics, and Frequency Control*, vol. 60, no. 9, pp. 1816–1826, Sep 2013.

[28] B. Byram, K. Dei, J. Tierney, and D. Dumont, "A model and regularization scheme for ultrasonic beamforming clutter reduction," *IEEE Transactions on Ultrasonics, Ferroelectrics, and Frequency Control*, vol. 62, no. 11, pp. 1913–1927, November 2015.

[29] J. Shin and L. Huang, "Spatial prediction filtering of acoustic clutter and random noise in medical ultrasound imaging," *IEEE Transactions on Medical Imaging*, vol. PP, no. 99, pp. 1–1, 2016.

[30] Jeremy J Dahl and Thomas J Feehan, "Direction of arrival filters for improved aberration estimation," *Ultrasonic imaging*, vol. 30, no. 1, pp. 1–20, 2008.

[31] Pai-Chi Li and Meng-Lin Li, "Adaptive imaging using the generalized coherence factor," *IEEE Transactions on Ultrasonics, Ferroelectrics, and Frequency Control*, vol. 50, no. 2, pp. 128–141, Feb 2003.

[32] J. Camacho, M. Parrilla, and C. Fritsch, "Phase coherence imaging," *IEEE Transactions on Ultrasonics, Ferroelectrics, and Frequency Control*, vol. 56, no. 5, pp. 958–974, May 2009.

[33] M. Karaman, Pai-Chi Li, and M. O'Donnell, "Synthetic aperture imaging for small scale systems," *IEEE Transactions on Ultrasonics, Ferroelectrics, and Frequency Control*, vol. 42, no. 3, pp. 429–442, May 1995.

[34] Billy Y.S. Yiu and Alfred C.H. Yu, "Gpu-based minimum variance beamformer for synthetic aperture imaging of the eye," *Ultrasound in Medicine and Biology*, vol. 41, no. 3, pp. 871 – 883, 2015.